frontiers | Frontiers in Earth Science

TYPE Original Research
PUBLISHED 15 June 2023
DOI 10.3389/feart.2023.1203157

OPEN ACCESS

EDITED BY
Songjian Ao,
Chinese Academy of Sciences (CAS), China

REVIEWED BY
Gaoxue Yang,
Chang'an University, China
Wei-Qiang Ji,
Chinese Academy of Sciences (CAS), China

*CORRESPONDENCE
Kai Weng,
kaikaino1@qq.com

RECEIVED 10 April 2023
ACCEPTED 02 June 2023
PUBLISHED 15 June 2023

CITATION
Weng K, Kang W, Zhao X, Ma Z, Cao J and Sui Q (2023), Petrogenesis, tectonic setting and geodynamic implications of keziergayin granites in the kelan basin (Chinese Altai): constraints from geochemistry, zircon U-Pb geochronology and Nd–Hf–Pb–O isotopes.
Front. Earth Sci. 11:1203157.
doi: 10.3389/feart.2023.1203157

Petrogenesis, tectonic setting and geodynamic implications of keziergayin granites in the kelan basin (Chinese Altai): constraints from geochemistry, zircon U-Pb geochronology and Nd–Hf–Pb–O isotopes

Kai Weng[1]*, Wenbin Kang[2], Xiaojian Zhao[1], Zhongping Ma[1], Jifei Cao[1] and Qinglin Sui[3]

[1]Key Laboratory for the Study of Focused Magmatism and Giant Ore Deposits MNR, Xi'an Center of Geological Survey, Xi'an, China, [2]School of Coal Engineering, Shanxi Datong University, Datong, China, [3]School of Resource Environment and Safety Engineering, University of South China, Hengyang, China

The Chinese Altai is characterized by abundant granitoids, which not only are indicators of the interaction between crust and mantle but also provide critical constraints on the tectonic evolution of the orogen. This study presents zircon U–Pb–O isotopes, whole-rock major and trace element and Nd–Hf–Pb isotopes data for granite porphyries from the Keziergayin region in the Kelan Basin. The granite porphyries intrude in the Kangbutiebao Formation with zircon U–Pb dating of 394 ± 3 Ma. They have the characteristics of subalkaline and metaluminous to weakly peraluminous and show geochemical affinity with I-type granite. The granite porphyry samples display negative $\varepsilon_{Nd}(t)$ (–1.9 to –1.4), positive $\varepsilon_{Hf}(t)$ (+4.3 to +11.4) values, with Nd–Hf decoupling; low Pb isotope compositions; $\delta^{18}O_{V\text{-}SMOW}$ (6.38‰–8.45‰) is less than 10‰, within the range of O isotopes of medium-basic igneous rocks. These geochemical signatures indicate that the granite porphyries originated from lower crust medium–basic igneous rocks extracted from the lithospheric mantle metasomatized by subducted melt. They are characterized by high SiO_2 contents and Rb/Sr ratios; low CaO contents and K/Rb ratios, hinting that they were formed by highly evolved magmas, with fractionation crystallization of feldspar, apatite, garnet, allanite and/or monazite. The granite porphyries possess positive Rb, Th, U, Nd, Zr, Pb and light rare Earth elements (LREEs) anomalies with strong negative Ba, Nb, Ta, Sr, P, Ti and Eu anomalies, implying that their formation were related to an island arc. Combined with previous studies, it is suggested that the existence of the Early Devonian arc-basin system associated with subducting slab rollback in the Chinese Altai, which belongs to the Siberian active continental margin system.

KEYWORDS

I-type granite, early devonian, slab rollback, Chinese Altai, continental growth

1 Introduction

The Central Asian Orogenic Belt (CAOB; Mossakovsky, 1993; Jahn et al., 2000b; Windley et al., 2007; Kröner et al., 2014; Zheng et al., 2015) is the largest Phanerozoic accretionary orogen in the world (Figure 1A; Zonenshain, 1990; Mossakovsky, 1993; Şengör et al., 1993; Jahn et al., 2000a, Jahn et al., 2000b; Windley et al., 2002; Windley et al., 2007). The CAOB extends from the Urals in the west to the Pacific in the east and from Siberia in the north to the North China and Tarim cratons in the south (Figure 1A; Zonenshain, 1990; Mossakovsky, 1993; Jahn et al., 2000a; Windley et al., 2007). It mainly developed from ca. 1,000 Ma to 250 Ma by the continuous, long-term subduction and accretion of multiple blocks of different origins, including island arcs, ophiolitic complexes, oceanic islands, seamounts, accretionary wedges, and oceanic plateaus (Coleman, 1989; Badarch et al., 2002; Khain et al., 2002; Zhu and Ogasawara, 2002; Xiao et al., 2004; Wilhem et al., 2012; Yang et al., 2015; 2022; Zhu et al., 2015), and substantial vertical addition of juvenile material derived from the upper mantle (Han et al., 1997; Jahn et al., 2000a; 2000b; Chen and Jahn, 2002; Jahn, 2004). Vertical crustal growth is supported by the study of isotopic geochemistry for the positive whole-rock $\varepsilon_{Nd}(t)$ and zircon $\varepsilon_{Hf}(t)$ values of granitoids in the CAOB (Han et al., 1997; Chen and Jahn, 2002; Jahn, 2004; Long et al., 2007; 2010; Yuan et al., 2007; Sun et al., 2008; Wang et al., 2009; Cai et al., 2011a; Cai et al., 2011b; Wang et al., 2023). These granitoids provide important constraints on the tectonic evolution of the CAOB and critical information on crustal growth (Jahn et al., 2000b; Jahn, 2004; Geng et al., 2009).

As a southwestern portion of the CAOB, the Chinese Altai is situated in the northern Xinjiang Uygur Autonomous Region of China and is composed of volcanic rocks, high-grade metamorphic rocks, sedimentary sequences, and voluminous granitoids (Windley et al., 2002; 2007). Granitoids and granitic gneisses occupy approximately 70% of the Chinese Altai (Windley et al., 2002), which is also an important rare metal and Fe-Cu-Ni metallogenic belt in China. The mineralization was closely related to the granitoids (Zhu et al., 2006; Chai et al., 2009). Recent zircon U–Pb isotopic dating results show that granitic magmatism continued from the Ordovician to Jurassic in the Chinese Altai and peaked ca. 400 Ma in the Early Devonian (Weng et al., 2023). The range of tectonic interpretations for these Early Devonian rocks is contradictory (Xiao et al., 2004; Long et al., 2007; Zhou et al., 2007), including an island arc related to subduction (Windley et al., 2002; Xiao et al., 2004), an active continental margin (Wang et al., 2006; Long et al., 2007; Liu et al., 2008; Yang et al., 2008), and a continental margin rift (Zhou et al., 2007).

Here, we carried out a detailed study on the major and trace elements, zircon U–Pb dating, zircon O isotope and whole-rock Nd–Hf–Pb isotopes for granite porphyries from the Kelan Basin in

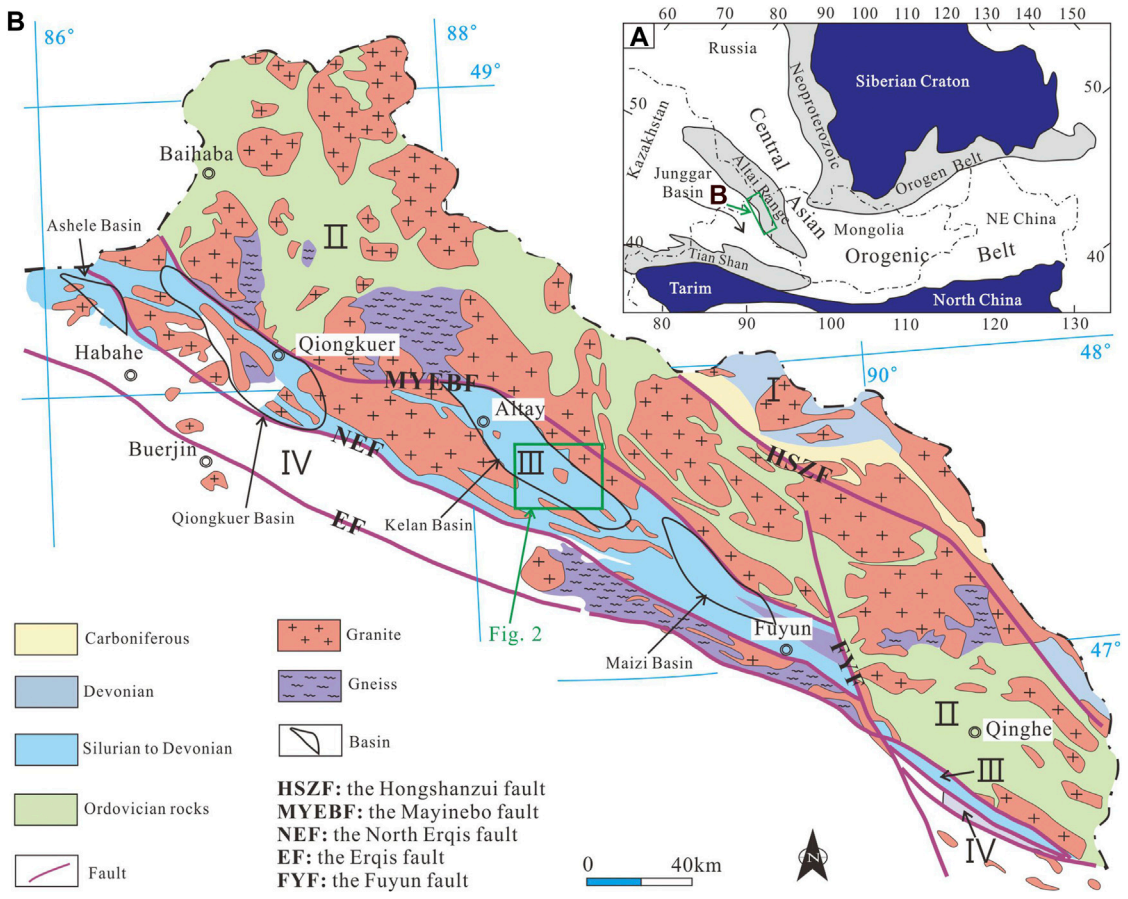

FIGURE 1
(A) Tectonic division of the CAOB, **(B)** geological map of the Chinese Altai (modified after Sun et al., 2009).

the Chinese Altai to unravel their petrogenesis and tectonic setting during the Early Devonian.

2 Regional geological setting

The Chinese Altai is in the central part of the CAOB, which separates the Kazakhstan and Junggar Blocks to the south and Siberian Craton to the north (Figure 1A; Wang et al., 2009; Zhang et al., 2017). Four domains bounded by faults can be identified in the Chinese Altai based on the analysis of magmatic activity, deformation, metamorphism and stratigraphy history (Figure 1B; Windley et al., 2002). Unit I (North Altai Domain) lies in the north of Altai, consisting of the upper Devonian to Carboniferous limestones and terrigenous clastic sediments, incorporating minor metamorphosed arc-related volcanic rocks; Unit II (Central Altai Domain) is located in the central Altai and bounded by the Hongshanzui fault from Unit I, consisting of a thick turbiditic and pyroclastic succession, middle to upper Silurian metasandstone and upper Ordovian volcanic molasse and clastic deposits of the Habahe Group; Unit III (Qiongkuer Domain) is separated from Unit II by the Mayinebo fault and located in the south of Altai, composed of arc-type volcano-sedimentary rocks of the lower Devonian Kangbutiebao Formation and an overlying middle–upper Devonian turbiditic sandstone–shale of the Altai Formation (Windley et al., 2002). The Kuerti mafic rocks are exposed at 30 km north of Fuyun County, which represent a suite of meta-basalts and meta-gabbros. The southern and northern blocks are separated by migmatitic gneiss belonging to the Kangbutiebao Group. In the north Kuerti block, layered meta-basalts dominate with a few gabbro and diabase dike or sheets intruding into the volcanic rock layers. In the south Kuerti block, the mafic rocks consist of an intrusive complex of gabbro and dolerite dikes and a few pillow basalts (Xu et al., 2003). Zircon SHRIMP U-Pb age of plagioclase granitic dikes in the gabbro unit of south Kuerti block is 372 ± 19 Ma (Zhang et al., 2003). Unit IV (Irtysh Domain) lies in the south of Altai and is separated from Unit III by the North Irtysh fault, composing a sequence of Devonian sediments and late Carboniferous volcaniclastic rock, with metamorphism at greenschist-to amphibolite-facies. Further south, the Chinese Altai is separated from the Junggar blocks by the Irtysh Fault (Figure 1B).

The granitoids in the Chinese Altai mainly occurred in the Paleozoic. These granitoids are classified into orogenic (462–375 Ma) and anorogenic (281–256 Ma) groups based on chemical compositions (Xiao et al., 2009). Geochemical studies have revealed that mantle-derived components as well as continental sources have both contributed to the generation of these granitoid magmas (Chen and Jahn, 2002; Wang et al., 2006; 2009; Yuan et al., 2007; Sun et al., 2008), and some magma chambers experienced composite assimilation and fractional crystallization processes (Liu et al., 1997).

3 Study area geology and sample collection

The granite porphyry samples were collected from the Keziergayin region in the Kelan Basin and intrude into the Kangbutiebao Formation. (Figure 2; Yang et al., 2017; Yang et al., 2019). The Kelan Basin lies in the Qiongkuer Domain (Figure 1B). The metamorphosed late Cambrian–early Ordovician rocks (495–481 Ma, Yang et al., 2017) and middle–late Silurian Kulumuti Group consist of migmatites, gneisses, granulite, schists and metasandstones and are exposed in the basement of the Kelan Basin (Figure 2A). The metamorphosed basement has a fault contact with arc-type volcano-sedimentary rocks of the lower Devonian Kangbutiebao Formation and an overlying middle–upper Devonian turbiditic sandstone–shale of the Altai Formation (Windley et al., 2002). The intrusions are widely distributed in and around the Kelan Basin and were emplaced during the middle Ordovian–late Triassic (462–202 Yang et al., 2021).

The granite porphyries are light red to dark gray in color and generally ~2 m wide and ~10 m long (Figure 2B; Figures 3A, B). The granite porphyries exhibit a gneissic structure (Figures 3A,B) and typical porphyritic texture (Figures 3C,D), and the mineral grains are mostly medium and fine. The phenocrysts (~15–20 vol%) mainly consist of alkaline feldspar (~5–10 vol%) and quartz (~10–15 vol%); the matrix (~80–85 vol%) with a fine-grained granitic texture contains a similar mineral assemblage of quartz (~33 vol%), K-feldspar (~27 vol%), plagioclase (~14 vol%), a small amount of biotite (~5.5 vol%), muscovite (~1 vol%), amphibole (~1 vol%) and opaque minerals (~1 vol%; Figures 3C,D). Accessory minerals are zircon and apatite. The alkaline feldspar phenocrysts are generally lath-shaped and form euhedral-subhedral grains with sizes up to 5 mm across. Abundant inclusions, such as biotite, can be locally observed in the alkaline feldspar (Figures 3C,D). The quartz phenocrysts are subhedral-anhedral in shape with sizes of ~0.1–7.5 mm in diameter (Figures 3C,D). Five granite porphyry samples were collected for this major and trace element, Nd–Hf–Pb–O isotopes and zircon U–Pb dating study.

4 Analytical methods

Zircon U–Pb geochronology, whole-rock geochemistry, Nd–Hf–Pb isotopes and zircon O isotope analyses were conducted on the samples collected in this study. Zircon U–Pb dating and O isotope have been completed at the Beijing Sensitive high-resolution ion microprobe (SHRIMP) Center. Whole-rock major and trace elements were determined at the Key Laboratory for the Study of Focused Magmatism and Giant Ore Deposits, the Xi'an Center of China Geological Survey, MNR. The whole-rock Nd and Pb isotope ratios were analyzed at the Beijing Research Institute of Uranium Geology, and the Hf isotope ratios were determined at the Institute of Geochemistry, Chinese Academy of Sciences.

4.1 Zircon U–Pb dating

After crushing, zircons were separated from 80 mesh sieved samples by standard heavy liquid and magnetic techniques. The representative zircons were handpicked and mounted with adhesive tape under a binocular microscope, enclosed in epoxy resin and polished to approximately half of their thickness. After being photographed under reflected and transmitted light, transmitted electron, backscattered electron (BSE) and cathodoluminescence (CL) images were obtained for zircons, revealing their internal structures.

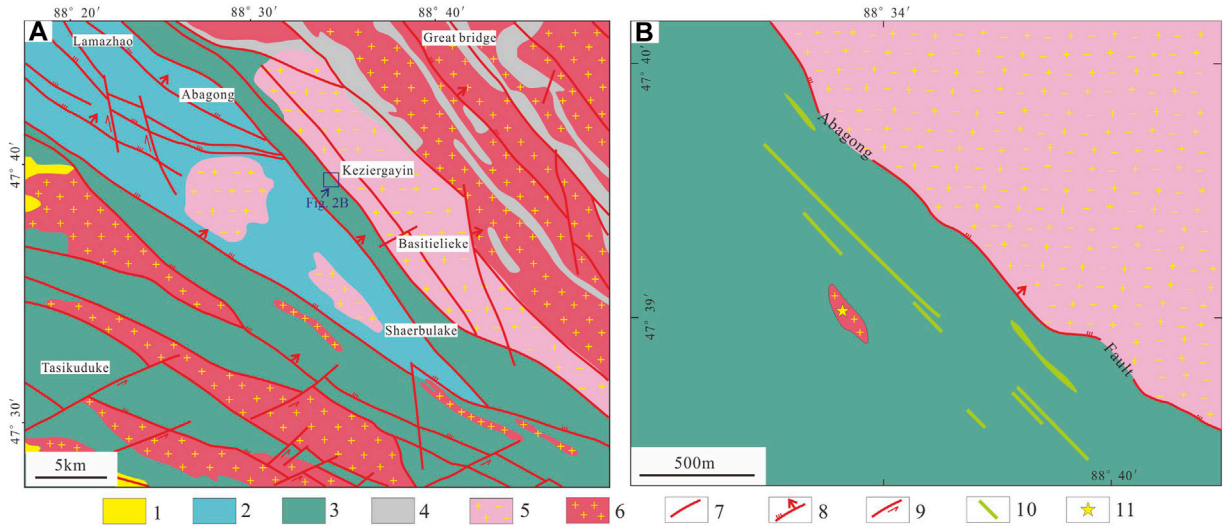

FIGURE 2
Simplified regional geological map of the Kelan basin **(A)** and Keziergayin region **(B)** in the Chinese Altai (after Yang et al., 2019; Bao et al., 2021). 1-Quaternary sediments; 2-Metasedimentary rocks of the Altay Formation; 3-Metavolcanosedimentary rocks of the Kangbutiebao Formation; 4-Late Cambrian–early Ordovician metamorphic rocks; 5-Permian granite; 6-Ordovician–Devonian granite; 7-Fault; 8-Compressoshear fault; 9-Shear fault; 10-Tungsten polymetallic ore body; 11-Location of sample.

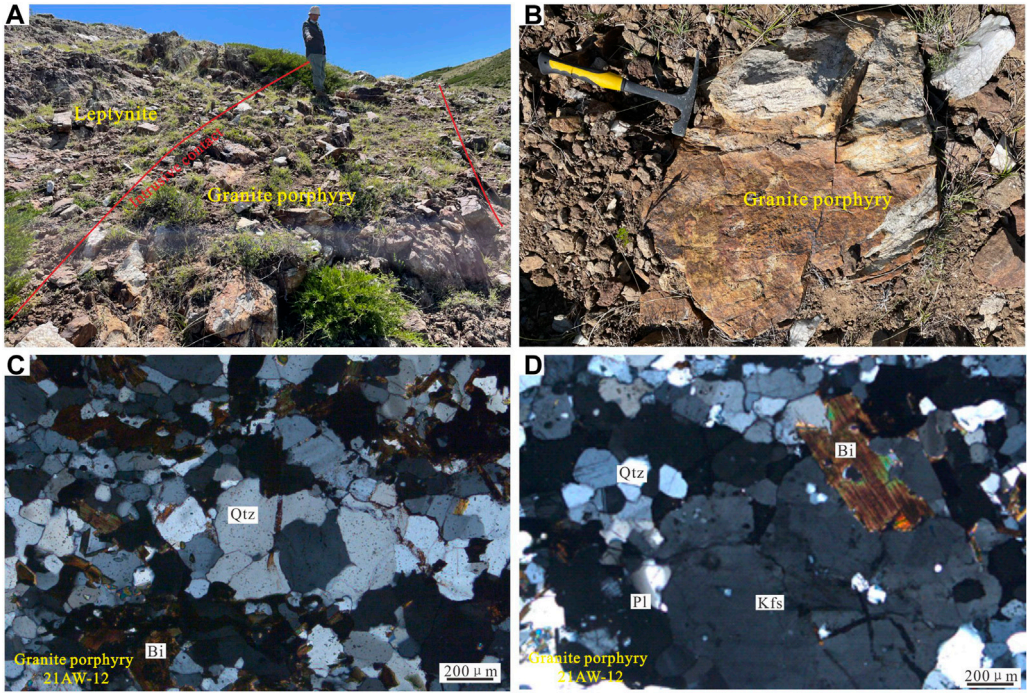

FIGURE 3
Field and microscopic photos of the granite porphyries from the Keziergayin region of the Kelan basin. **(A)** The leptynite of the Devonian Kangbutiebao Formation was intruded by granite porphyry. **(B)** Hand specimen of granite porphyry. **(C,D)** Mineral compositions and texture of granite porphyry (sample 21AW-12). Qtz=quartz, Pl=plagioclase, Kfs=K-feldspar, Bi= biotite.

In SHRIMP zircon U–Pb analyses, spot sizes were 25–30 μm, and the intensity of the primary particle flow was approximately 4 nA. Each data point measurement consisted of five scans. The interelement fractionation correction was carried out using standard zircon TEM (417 Ma). The standard zircon SL13 (572 Ma) was used to calibrate the contents of U, Th and Pb of the standard TEM

(417 Ma) and the analyzed zircons. The detailed analysis process followed that described by Song (2002). Ludwig SQUID 1.0 and Isoplot (Ludwig, 2003) were used for processing the original data and drawing the zircon U–Pb concordia diagrams.

4.2 Major and trace element analyses

Fresh samples for whole-rock analyses were collected and crushed to 200 mesh using an agate mill. Major elements were obtained by a Phillips PW 240 X-ray fluorescence (XRF) spectrometer on fused glass beads. The analytical precision was better than 1%. Trace elements were analyzed by an inductively coupled plasma mass spectrometry (ICP–MS) using an Agilent 7,700×ICP–MS system, and the accuracies for minor element content were better than 5%. For a detailed analytical process, please refer to those described by Ma et al. (2012) and Gao et al. (2008).

4.3 Whole-rock Nd–Hf–Pb isotopic analyses

About 0.1 g powder sample was accurately weighed in a low-pressure sealed sample dissolving tank, diluent Sm-Nd was accurately added, and dissolved with mixed acid ($HF+HNO_3+HClO_4$) for 24 h. After the sample was completely dissolved, it was steamed and dried by adding 6 mol/L hydrochloric acid into chloride. The solution was dissolved in 0.5 mol/L hydrochloric acid solution and centrifuged. The clear solution was placed in cation-exchange column (φ0.5×15 cm, AG50W×8 (H+) 100–200 mesh). The matrix elements and other elements were rinsed with 1.75 mol/L hydrochloric acid solution and 2.5 mol/L hydrochloric acid solution. The rare Earth elements were washed with 4 mol/L hydrochloric acid solution and then dried. Sm-Nd were separated using P507 extraction resin, evaporated to dryness, and converted into nitrate for mass spectrometry analysis. Nd isotopic analysis was performed using an ISOPROBE-T thermal ionization mass spectrometer. The mass fractionation correction of Nd isotopes was based on a $^{146}Nd/^{144}Nd$ ratio of 0.7219, and the JMC standard $^{143}Nd/^{144}Nd=0.512109 \pm 3$ was used by an experimental monitor. The background Sm and Nd concentrations of the whole analytic process are less than 50 pg.

About 0.1 g powder sample was accurately weighed in a savillex sample dissolving tank, 3 mL of mixed acid solution of $HF:HNO_3=3:1$ was added. The samples were heated on an electric heating plate using a temperature of 120°C for 3 days to dry the sample. Then, 3 mL HNO_3 was added, followed by evaporation to dry the sample, then 3 mL 6N HCl was added, then evaporation to dry again, and finally 2N HF was added to dissolve the sample, loaded on an ion-exchange column for separation, and prepared for analyses. Hf isotope analysis was performed by Neptune Plus type MC-ICP-MS. The instrumental fractionation of Hf isotopes was monitored by measuring the Hf standard solution JMC475 every 15 samples. The Hf isotope data was normalized to $^{179}Hf/^{177}Hf=0.7325$ using the exponential law. The mean $^{176}Hf/^{177}Hf$ for JMC 475 solutions in this study was 0.282163 ± 13 (2δ, n=7).

About 0.1–0.2 g powder sample was accurately weighed in a low-pressure sealed sample dissolving tank, and dissolved with mixed acid ($HF+HNO_3+HClO_4$) for 24 h. After the sample was completely dissolved, it was steamed and dried by adding 6 mol/L hydrochloric acid into chloride. The solution was dissolved in 1 mL 0.5 mol/L HBr solution and centrifuged. The clear solution was placed in anion-exchange column (250 μL AG1×8,100–200 mesh). The impurities were washed with 0.5 mol/L HBr, and the lead was parsed with 1 mL 6 mol/L HCl in a Teflon beakers, then dried for use. Pb isotopic analysis was performed using an ISOPROBE-T thermal ionization mass spectrometer. Pb isotopic analysis was corrected using NBS981 as the reference material, and its uncorrected results was $^{208}Pb/^{206}Pb=2.164940 \pm 15$, $^{207}Pb/^{206}Pb=0.914338 \pm 7$, $^{204}Pb/^{206}Pb=0.0591107 \pm 2$ and the whole process background Pb<100 pg.

4.4 Zircon O isotopic analyses

In situ zircon O isotope analyses were conducted on the same zircon spots as U–Pb laser ablation with a 25 μm spot. The zircon TEMORA 2 ($\delta^{18}O=8.20‰$) standard was measured as an unknown to monitor the external precision, and the analysis point ratio of the standard sample and analysis sample was 1:3. The measured values of a single point are the calculated mean value of $^{18}O/^{16}O$ with 10 groups of scans, and the accuracy of single point $^{18}O/^{16}O$ data is generally better than 0.2‰–0.3‰. Details of the instrumental conditions and data acquisition procedures were similar to those described by Ávila et al. (2020).

5 Results

5.1 Zircon morphology and U–Pb geochronology

Zircon grains from the granite porphyry (21 AW-12) were selected for U–Pb dating, as summarized in Table 1. Zircon grains in the sample display colorless and transparent grains in plane-polarized light, exhibiting euhedral–subhedral shapes. Their lengths range from 75–135 μm, and the length/width ratios range from 2:1–3:1. Under CL images, most zircon grains are prismatic and weakly to moderately luminescent with typical oscillatory zoning, hinting at a magmatic origin (Figure 4A). Twelve spots were analyzed on 12 zircon grains from sample 21AW-12. They have high Th/U ratios greater than 0.46 (Table 1). Twelve analyses with better concordant $^{206}Pb/^{238}U$ ages ranging from 385 Ma to 404 Ma yield a weighted mean age of 394 ± 3 Ma (2σ, MSWD=1.14; Figures 4B,C), which is Early Devonian, representing the emplacement age of magma.

5.2 Whole-rock major and trace elements

Five samples of the granite porphyry were analyzed to acquire their major and trace element compositions, as summarized in Table 2 and illustrated in Figures 5, 6. The granite porphyry samples are characterized by high SiO_2 (74.69–82.08 wt%) and Na_2O (3.59–6.12 wt%) concentrations, moderate Al_2O_3 (10.13–14.99 wt%), and low FeO^T (0.44–0.88 wt%), MgO (0.05–0.2 wt%) and CaO (0.42–3.8 wt%) with low K_2O/Na_2O

10.3389/feart.2023.1203157

TABLE 1 SHRIMP U–Pb geochronological data of single zircons from granite porphyries.

Sample/ zircon number	$^{206}Pb_c$(%)	U (ppm)	Th (ppm)	Th/ U	$^{206}Pb^*$ (ppm)	$^{206}Pb/^{238}U$	% err	$^{207}Pb/^{206}Pb$	% err	$^{206}Pb/^{238}U$ age (Ma)	1σ err	$^{207}Pb/^{206}Pb$ age (Ma)	1σ err	% Dis
21AW-12 (Sample number)														
Zr.1	0.00	581	303	0.54	31.7	0.06341	1.3	0.05455	1.4	396	5	394	32	−1
Zr.2	0.53	680	328	0.50	37.5	0.06382	1.3	0.05230	2.6	399	5	297	59	−34
Zr.3	0.07	461	322	0.72	25.1	0.06331	1.3	0.05499	1.8	396	5	412	39	4
Zr.4	0.10	517	278	0.56	27.9	0.06277	1.3	0.05544	1.8	393	5	430	40	9
Zr.5	0.24	551	269	0.50	29.3	0.06163	1.3	0.05450	2.2	386	5	391	49	1
Zr.6	--	481	226	0.49	26.7	0.06474	1.3	0.05549	1.6	404	5	432	35	6
Zr.7	0.10	586	347	0.61	31.7	0.06292	1.3	0.05416	1.5	393	5	378	33	−4
Zr.8	0.00	670	403	0.62	35.4	0.06151	1.3	0.05358	1.4	385	5	354	31	−9
Zr.9	0.89	722	323	0.46	39.2	0.06263	1.3	0.05490	2.8	392	5	407	63	4
Zr.10	0.19	441	224	0.53	24.1	0.06359	1.4	0.05390	2.3	397	5	366	51	−8
Zr.11	0.16	498	250	0.52	27.1	0.06338	1.3	0.05420	2.5	396	5	378	57	−5
Zr.12	0.20	560	313	0.58	30.6	0.06334	1.4	0.05408	1.7	396	5	375	38	−6

Errors are 1-sigma; Pbc and Pb* indicate the common and radiogenic portions, respectively.
Common Pb corrected using measured ^{204}Pb.

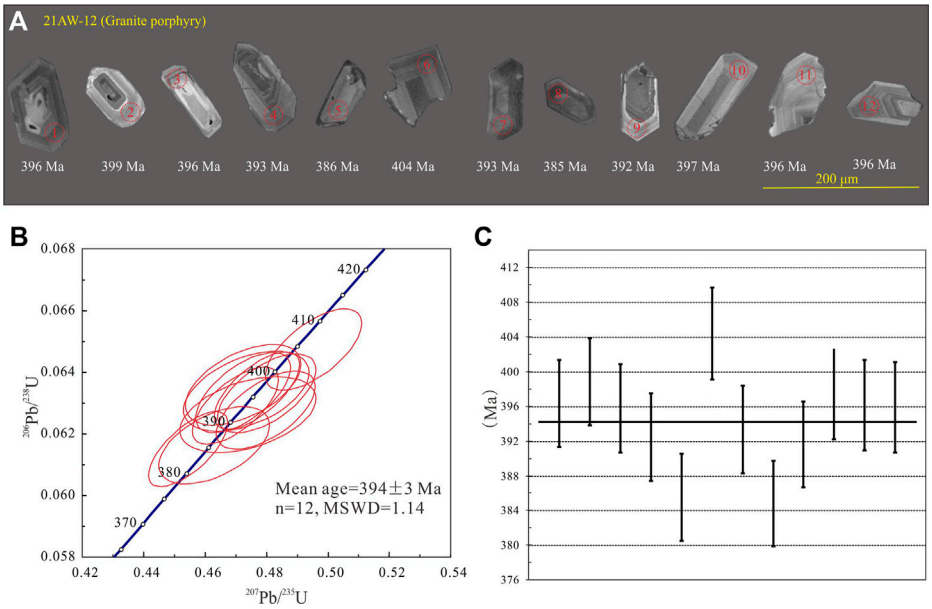

FIGURE 4
CL images **(A)**, U–Pb concordia diagrams **(B)** and $^{206}Pb/^{238}U$ mean ages **(C)** of zircon grains for granite porphyry samples from the Keziergayin region.

ratios between 0.04 and 1.03, and $Mg^{\#}$ ($Mg^{\#}$=100*(MgO/40.3044)/(MgO/40.3044+FeO^T/71.844) values of 9–32 (Figure 5; Table 2). The granite porphyries have low alkalis (Na_2O+K_2O=4.91–7.29 wt%); on a total alkalis vs. silica (TAS) diagram, they plot in the granite field with a subalkaline signature (Figure 6A); on a K_2O vs. SiO_2 diagram, the granitic rock samples show an evolution trend from a low-K (tholeiite) series to a high-K calc-alkaline series (Figure 6B). They show weakly peraluminous and metaluminous signatures with aluminum saturation indices of A/CNK and A/NK ranging from 0.98 to 1.02 and from 1.06 to 1.88, respectively (Figure 6C).

TABLE 2 Whole-rock major and trace element compositions of granite porphyries.

Samples elements	21AW-12	21AW-13	21AW-14	21AW-15	21AW-16
SiO_2	77.10	80.29	82.08	74.69	77.67
Al_2O_3	12.76	11.42	10.13	14.99	12.36
Fe_2O_3	0.50	0.16	0.31	0.62	0.26
FeO	0.30	0.30	0.31	0.32	0.25
CaO	1.31	0.48	0.42	3.80	1.38
MgO	0.20	0.08	0.09	0.05	0.10
K_2O	1.66	0.63	1.42	0.19	3.70
Na_2O	5.37	6.12	4.66	4.72	3.59
TiO_2	0.19	0.11	0.11	0.13	0.13
P_2O_5	0.03	0.02	0.02	0.02	0.02
MnO	0.06	0.02	0.02	0.04	0.02
LOI	0.45	0.32	0.33	0.35	0.41
Cu	90.7	66.2	35.8	66.6	80.1
Pb	10.9	3.57	3.36	9.24	9.52
Zn	27.0	8.61	11.1	38.2	322
Ni	6.05	2.88	3.12	4.10	3.86
Co.	2.32	0.880	0.660	0.820	0.850
Li	9.59	2.15	2.11	2.85	5.83
Rb	65.1	18.5	29.4	10.3	139
Cs	1.47	0.540	0.520	0.410	5.20
W	19.7	3.12	2.45	5.24	8.39
Mo	4.98	1.33	1.44	7.00	6.81
Sr	70.5	33.9	33.5	315	243
Ba	169	56.6	101	59.7	383
V	6.07	0.860	2.04	2.77	2.65
Sc	7.42	6.13	5.72	5.25	1.81
Nb	11.6	9.53	8.18	6.93	9.78
Ta	1.46	1.01	0.960	0.910	1.03
Zr	123	109	94.2	108	134
Hf	5.05	4.04	3.48	3.69	4.71
Ga	12.8	10.4	11.2	20.8	11.2
Sn	3.98	3.03	3.98	6.04	4.55
U	4.80	3.17	2.42	1.75	2.00
Th	12.8	12.9	13.4	16.6	13.2
La	40.3	21.7	60.8	12.0	6.62
Ce	96.1	48.7	131	22.8	13.8
Pr	11.1	6.31	16.6	3.05	1.81
Nd	42.4	23.9	61.6	11.5	7.18
Sm	9.70	5.62	11.4	2.84	1.92
Eu	1.17	0.740	1.42	0.370	0.290
Gd	7.73	5.26	8.10	2.85	1.95
Tb	1.17	0.980	1.22	0.550	0.390
Dy	6.18	6.20	5.98	3.65	2.74
Ho	1.27	1.36	1.16	0.760	0.640
Er	3.89	3.94	3.22	2.34	2.12
Tm	0.640	0.590	0.480	0.330	0.360
Yb	4.35	3.83	3.26	2.18	2.55
Lu	0.670	0.560	0.480	0.330	0.450
Y	31.8	31.3	30.6	19.1	15.5

(Continued in next column)

The granite porphyries have low total rare Earth elements (REEs) contents of 42.82–306.72 ppm Table 2. In the chondrite-normalized REEs distribution diagram (Figure 7A), the granite porphyry samples display enrichments in light REEs (LREEs) ($(La/Yb)_N$ =1.86–13.38) and flat heavy REEs (HREEs) ($(Dy/Yb)_N$=0.72–1.23) with obviously negative Eu anomalies (δEu=0.40–0.46). On the primitive mantle-normalized multielement diagram, the granite porphyry samples show negative Ba, Sr, Nb, Ta, P and Ti and positive Rb, Th, U, Nd, Zr and Pb anomalies (Figure 7B).

5.3 Whole-rock Nd–Hf–Pb isotopes

Four samples of the granite porphyry were further chosen to acquire their Nd–Hf–Pb isotopes, as listed in Tables 3–5. The results of initial $^{143}Nd/^{144}Nd$ ratios, $\varepsilon_{Nd}(t)$, $\varepsilon_{Hf}(t)$, initial $^{206}Pb/^{204}Pb$, initial $^{207}Pb/^{204}Pb$, and $^{208}Pb/^{204}Pb$ were calculated at t=394 Ma based on the results of zircon U–Pb dating. The granite porphyries exhibit low initial $^{143}Nd/^{144}Nd$ (0.512033–0.512059), negative $\varepsilon_{Nd}(t)$ (−1.9 to −1.4) values, with T_{2DM} Nd model ages of 1,438–1774 Ma (n=4; Table 3; Figure 8A), positive $\varepsilon_{Hf}(t)$ (+4.3 to +11.4) values, T_{2DM} Hf model ages of 661–1,112 Ma (n=4; Table 4; Figure 8B), and low $(^{206}Pb/^{204}Pb)_i$ (17.363–18.408), $(^{207}Pb/^{204}Pb)_i$ (15.515–15.557) and $(^{208}Pb/^{204}Pb)_i$ (36.953–37.696) values (n=4; Table 5; Figure 8D).

5.4 Zircon O isotope

Twelve zircon grains for granite porphyry that were used for U–Pb dating were further chosen to determine their $\delta^{18}O_{V\text{-}SMOW}$ values. The results are summarized in Table 6 and presented in

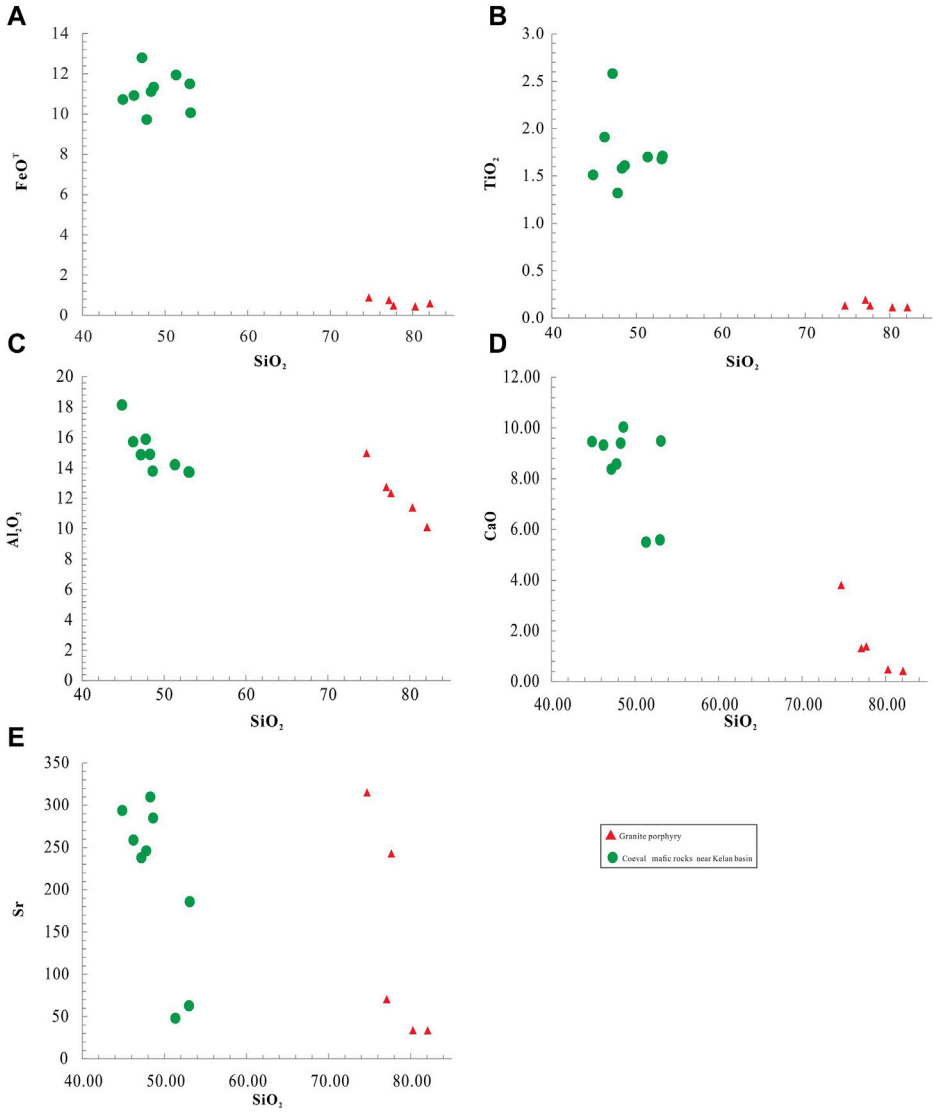

FIGURE 5
(A–D) SiO_2 *versus* selected major element oxides (wt%); **(E)** Variations diagram of SiO_2 (wt%) *versus* Sr (ppm). Data from coeval mafic rocks from the North Kuerti block reported in Xu et al. (2003) are shown for comparison.

Figure 8E. The magmatic zircons from granite porphyry display $\delta^{18}O_{V\text{-}SMOW}$ values of 6.38‰–8.45‰, with an average of 7.14‰.

6 Discussion

6.1 Genetic classification

In general, granites can be divided into S-, I- and A-types according to their mineralogical and geochemical characteristics and the nature of their protoliths (Collins et al., 1982; Whalen et al., 1987; Chappell and White, 1992; Wang S J et al., 2020). I-type granites are metaluminous to weakly peraluminous and commonly contain amphibole as a diagnostic phase (Chappell et al., 2012); S-type granites are strongly peraluminous and contain cordierite, muscovite and other aluminum-rich minerals. Chappell (1974) proposed that the boundary between S-type and I-type granites can be drawn at an A/CNK ratio of 1.1. There is a small amount of muscovite in the petrographic observations of granite porphyry samples. In contrast, the extremely low P_2O_5 content (0.002–0.003 wt%), weakly peraluminous and metaluminous signatures with the moderate A/CNK content in geochemical analysis indicate that S-type granites can be excluded (Chappell, 1974; King et al., 1997; Bonin, 2007). Geochemically, the granite porphyries show lower Zr (94.2–134.0 ppm), Nb (6.9–11.6 ppm), total REEs (42.8–306.7 ppm), Zr+Nb+Y+Ce (156.8–264.0 ppm) and Ga/Al ratio (10,000×Ga/Al ratios of 1.71–2.62) values than typical A-type granite (Collins et al., 1982; White and Chappell, 1983; Whalen et al., 1987; Zhao et al., 2018). In the discrimination diagrams of FeO^T/MgO, Zr, Ce vs. 10,000 Ga/Al (Figures 9A–C), they plot in the fields

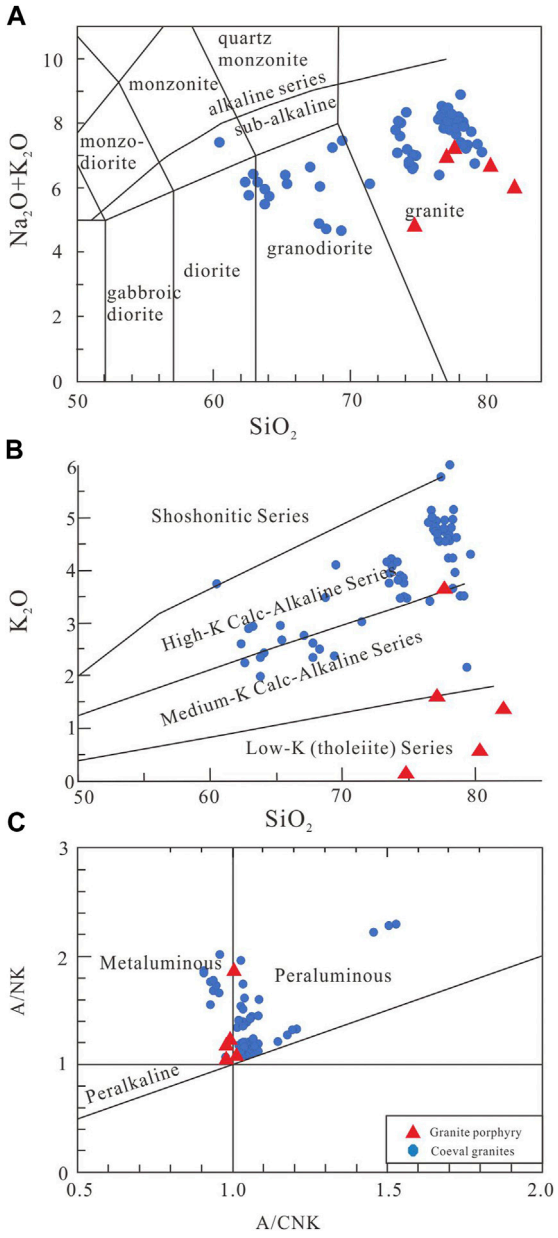

FIGURE 6
Plots of **(A)** SiO_2 *versus* Na_2O+K_2O (after Irvine and Baragar, 1971; Middlemost, 1994), **(B)** SiO_2 *versus* K_2O (after Peccerillo and Taylor, 1976), and **(C)** A/CNK *versus* A/NK (after Maniar and Piccoli, 1989) for granite porphyries and other early Devonian granitoids of the Chinese Altai. Other Early Devonian granitoid data are from Jiang (2021), Zheng et al. (2015), Tian (2018) and Yu et al. (2017). A/CNK=molarAl_2O_3/($CaO+Na_2O+K_2O$), A/NK=molarAl_2O_3/(Na_2O+K_2O).

straddling between I- and S-types and A-type granite. In the FeO^T/MgO vs. (Zr+Nb+Ce+Y) diagram (Figure 9A), they plot in the fields straddling fractionated and unfractionated I- and S-type granites. Therefore, the granite porphyries are not typical A-type granites but fractionated I-type granites.

6.2 Magmatic source

I-type granitic melts can originate from different source (Holden et al., 1987; Han et al., 1997; Griffin et al., 2002; Bonin, 2007; Zhong et al., 2007; Yang et al., 2008; Ahmed et al., 2018; Chen et al., 2018; Wang J et al., 2020), including mantle-derived magma, magma mixing or mingling of mafic and felsic magmas, and mafic to intermediate igneous rocks (Li et al., 2007; Chappell et al., 2012; Wang S J et al., 2020). The granite porphyries in this study contain low contents of MgO, FeO^T, $Mg^{\#}$ and Ni (Table 2), and no mafic–ultramafic cumulates occur in association with granitic intrusions as synplutonic dikes (Gao et al., 2016). In Figure 5, they show no linear trends with coeval mafic igneous rocks from the North Kuerti area (Xu et al., 2003; Shen et al., 2017), indicating different origins between the granitic and mafic rocks. These geochemical characteristics argue against the formation of granite porphyries originated from mantle-derived magma. The granite porphyries have a narrow range of whole-rock Nd compositions (Figure 8A; Table 3). Mafic magmatic enclaves that commonly occur as indicators of magma mixing or mingling are also not observed in the granite porphyries. Thus, a model of crust and mantle mixing is not favored for the origin of the magma. In contrast, their $\delta^{18}O_{V\text{-}SMOW}$ values are 6.38‰–8.45‰, less than 10‰, within the range of O isotope of medium–basic igneous rocks (Figure 8E), suggesting that the magma of the granite porphyries was derived from mafic to intermediate igneous rocks (Li et al., 2007; Chappell et al., 2012; Wang J et al., 2020).

These samples show geochemical signatures of negative ε_{Nd} (t) (−1.9 to −1.4) and positive ε_{Hf} (t) (+4.3 to +11.4) values (Figures 8A,B). In the diagram of ε_{Nd} (t) and ε_{Hf} (t), they plot in the fields straddling ocean island basalt (OIB) and global lower crust and mainly in the fields of global lower crust, supporting a lower crust origin (Figure 8C). Significant Nd-Hf isotope decoupling was shown by all samples in this study (Figure 8C), which may have resulted from disequilibrium melting processes or inherited from the magma source (Yu et al., 2017). However, the poor correlation between the Hf and $\varepsilon_{Hf}(t)$ values rule out the former model (Farina et al., 2014; Figure 10A). Therefore, the decoupled Nd–Hf isotopic features of the granite porphyries should be inherited from the magma source and may reflect the previous subduction process (Jiang et al., 2006), consistent with the geochemical characteristics of enrichment of Rb, Th and U and depletion of Nb, Ta, P and Ti in the primitive mantle-normalized trace element spider diagrams (Figures 7A,B). Because subduction slab-derived melts possessing high Nd/Hf ratios may add to the lithospheric mantle and result in Nd–Hf isotopic decoupling in the mantle (Pearce et al., 1999; Spandler et al., 2007; Todd et al., 2010), magma sources might be extracted from the lithospheric mantle and inherited Nd–Hf isotopic decoupling features of the mantle (Yu et al., 2017). This crust-mantle interconnection is further supported by the Pb isotope compositions of the granite porphyries that plot between the orogenic and mantle lines near the orogenic line (Figure 8D). Thus, the granite porphyries are interpreted to originate from lower crust medium–basic igneous rocks extracted from the lithospheric mantle metasomatized by subducted melt.

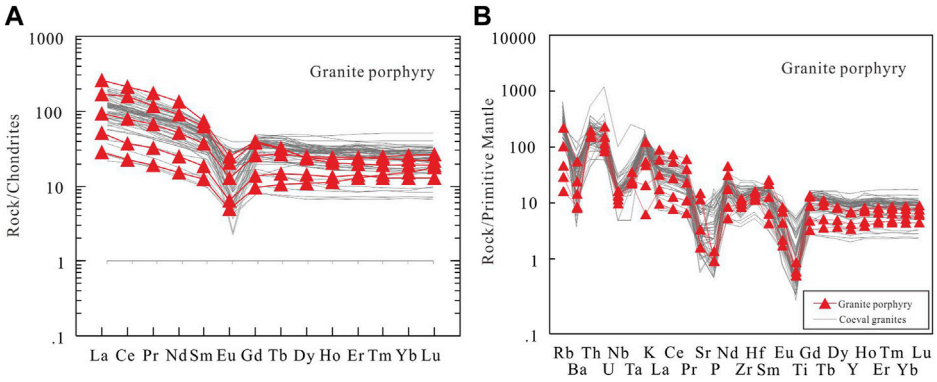

FIGURE 7
(A) Chondrite-normalized rare Earth elements (REEs) patterns and **(B)** primitive mantle-normalized multielement variation diagrams for granite porphyries. The chondrite values and primitive mantle values are after Taylor and McLennan (1985) and Sun and McDonough (1989), respectively. Other Early Devonian granitoid data are from Jiang (2021), Zheng et al. (2015), Tian (2018) and Yu et al. (2017).

TABLE 3 Whole-rock Nd isotope composition of granite porphyries.

Samples	Sm (ppm)	Nd (ppm)	$^{147}Sm/^{144}Nd$	$^{143}Nd/^{144}Nd$	t (Ma)	$(^{143}Nd/^{144}Nd)_i$	$\varepsilon_{Nd}(t)$	T_{DM}(Ma)	T_{2DM}(Ma)
21AW-12	9.70	42.40	0.1392	0.512394	394	0.512035	−1.9	1,545	1,446
21AW-13	5.62	23.90	0.1431	0.512428	394	0.512059	−1.4	1,556	1,438
21AW-15	2.84	11.50	0.1503	0.512443	394	0.512055	−1.5	1,696	1,526
21AW-16	1.92	7.18	0.1628	0.512453	394	0.512033	−1.9	2078	1774

The $^{147}Sm/^{144}Nd$ ratios of samples were calculated based on Sm and Nd content. $T_{DM} = 1/\lambda\ln[[(^{143}Nd/^{144}Nd)_s-(^{143}Nd/^{144}Nd)_{DM}]/[(^{147}Sm/^{144}Nd)_s-(^{143}Sm/^{144}Nd)_{DM}]+1]$; $T_{2DM} = T_{DM}-(T_{DM-t})*(f_{cc}-f_s)/(f_{cc}-f_{DM})$; In the formula, the subscript s and DM represent the analytical values of samples and the values of depleted mantle, respectively $(^{143}Nd/^{144}Nd)_{DM} = 0.51315$, $(^{147}Sm/^{144}Nd)_{DM} = 0.2137$, $\lambda = 6.54 \times 10^{-12}$ a^{-1}, $f_s = (^{147}Sm/^{144}Nd)_s/(^{147}Sm^{144}Nd)_{CHUR}-1$, $(^{147}Sm/^{144}Nd)_{CHUR} = 0.1967$, $f_{cc} = -0.4$, $f_{DM} = 0.08592$.

TABLE 4 Whole-rock Hf isotope composition for granite porphyries.

Samples	Lu (ppm)	Hf(ppm)	$^{176}Lu/^{177}Hf$	$^{176}Hf/^{177}Hf$	t (Ma)	$(^{176}Hf/^{177}Hf)_i$	$\varepsilon_{Hf}(t)$	T_{DM}(Ma)	T_{2DM}(Ma)
21AW-12	0.67	5.05	0.01880	0.282909	394	0.282770	8.6	925	838
21AW-13	0.56	4.04	0.01964	0.282921	394	0.282776	8.8	932	825
21AW-15	0.33	3.69	0.01267	0.282942	394	0.282848	11.4	638	661
21AW-16	0.45	4.71	0.01354	0.282748	394	0.282648	4.3	1,072	1,112

$T_{DM} = 1/\lambda\ln[[(^{176}Hf/^{177}Hf)_s-(^{176}Hf/^{177}Hf)_{DM}]/[(^{176}Lu/^{177}Hf)_s-(^{176}Lu/^{177}Hf)_{DM}]+1]$; $T_{2DM} = T_{DM}-(T_{DM}-t)*(f_{cc}-f_s)/(f_{cc}-f_{DM})$; In the formula, the subscript s and DM represent the analytical values of samples and the values of depleted mantle, respectively $(^{176}Lu/^{177}Hf)_{DM} = 0.0384$, $(^{176}Hf/^{177}Hf)_{DM} = 0.28325$, $\lambda = 1.867 \times 10^{-11}$ a^{-1}, $f_s = (^{176}Lu/^{177}Hf)_s/(^{176}Lu/^{177}Hf)_{CHUR}-1$, $(^{176}Lu/^{177}Hf)_{CHUR} = 0.0332$, $f_{cc} = -0.55$, $f_{DM} = 0.16$.

TABLE 5 Whole-rock Pb isotope composition for granite porphyries.

Samples	Pb(ppm)	U (ppm)	Th (ppm)	t (Ma)	$^{206}Pb/^{204}Pb$	±2σ	$^{207}Pb/^{204}Pb$	±2σ	$^{208}Pb/^{204}Pb$	±2σ	$(^{206}Pb/^{204}Pb)_i$	$(^{207}Pb/^{204}Pb)_i$	$(^{208}Pb/^{204}Pb)_i$
21AW-12	10.90	4.80	12.80	394	19.331	0.063	15.622	0.474	39.347	0.020	17.363	15.515	37.696
21AW-13	3.57	3.17	12.90	394	21.765	0.063	15.765	0.474	42.586	0.020	17.797	15.549	37.505
21AW-15	9.24	1.75	16.60	394	19.015	0.063	15.603	0.474	39.479	0.020	18.169	15.557	36.953
21AW-16	9.52	2.00	13.20	394	19.347	0.063	15.608	0.474	39.178	0.020	18.408	15.557	37.228

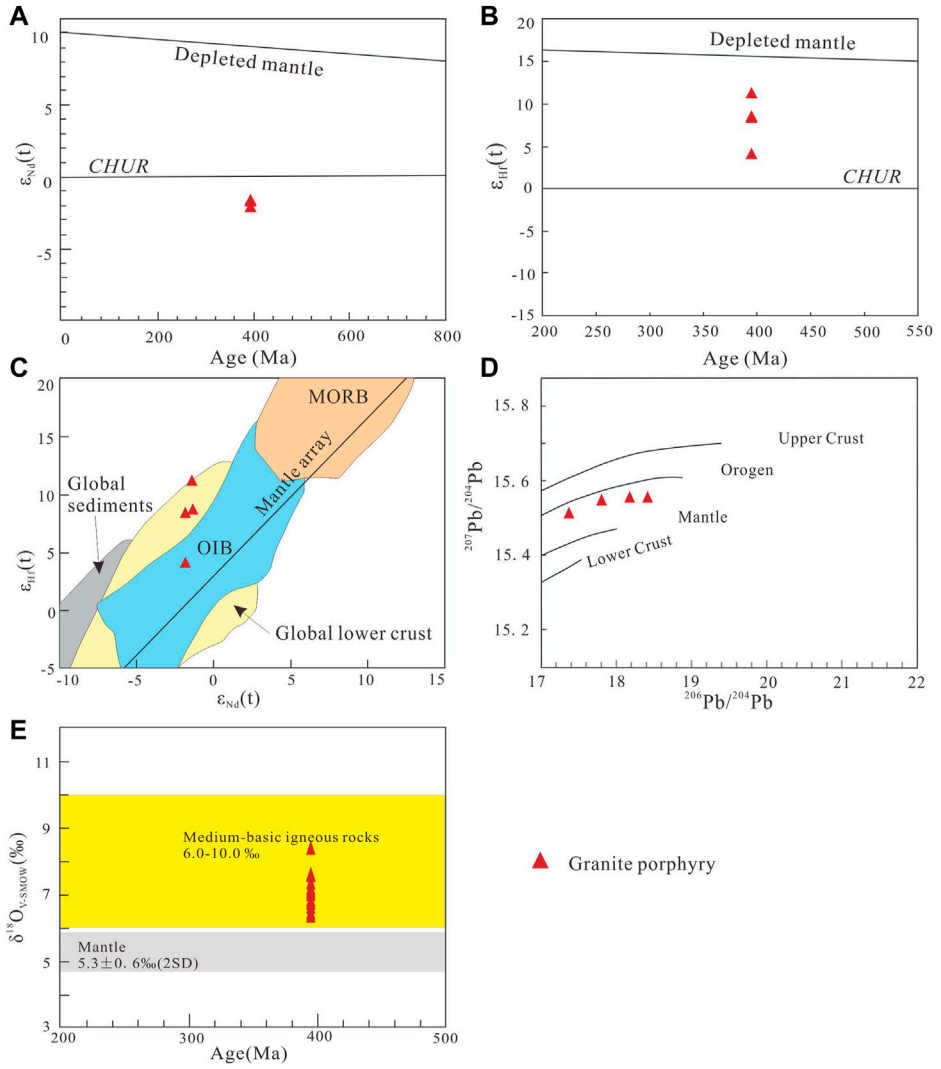

FIGURE 8
Age *versus* $\varepsilon_{Nd}(t)$ **(A)** and $\varepsilon_{Hf}(t)$ **(B)** diagrams, $\varepsilon_{Nd}(t)$ *versus* $\varepsilon_{Hf}(t)$ diagram **(C)**, $^{206}Pb/^{204}Pb$ *versus* $^{207}Pb/^{204}Pb$ diagram **(D)**, and age *versus* $\delta^{18}O_{V\text{-}SMOW}$ diagram **(E)**.

6.3 Magmatic evolution

The granite porphyries show geochemical characteristics of high SiO_2 contents and Rb/Sr ratios, low CaO contents and K/Rb ratios, and strong negative Eu anomalies, hinting that they were formed by highly evolved magmas (Table 2) and were mainly controlled by a fractionation crystallization process. The negative P anomaly could be resulting from high differentiation of apatite. Pronounced negative anomalies of Eu, Ba and Sr could result from crystal fractionation of feldspar. Separation of both plagioclase and K-feldspar can be conjectured from the Sr decrease with increasing Rb/Sr ratio (Figure 10B). The TiO_2 and FeO^T contents show a negative correlation with increasing SiO_2 (Figures 5A,B), indicating crystal fractionation of Fe-Ti oxides. Separation of crystallized rutile may be the main cause for the decreasing titanium content in granite porphyries (Figure 10C). Moreover, the granite porphyries have decreasing LREEs contents corresponding to crystal fractionation of allanite and/or monazite (Figure 10D), consistent with the geochemical characteristics of scattered LREEs in the chondrite-normalized REEs distribution (Jahn et al., 2001).

6.4 Tectonic setting and geodynamic implication

6.4.1 Tectonic setting

The Early Devonian granite porphyries are low-K calc-alkaline and metaluminous to weakly peraluminous in composition (Figure 6), with negative Ba, Sr, Nb, Ta, P, Eu and Ti anomalies and positive light REEs, Rb, Th, U, Nd, Zr and Pb anomalies (Figure 7). Within the element tectonic discrimination diagrams, the granite porphyries plot in the volcanic arc granite (VAG) field (Figure 11). These granites

TABLE 6 The O isotope compositions of zircon grains for granite porphyries.

Sample number	Zircon number	$\delta^{18}O_{V\text{-}SMOW}$ (‰)
12AW-12	Zr.1	6.89
	Zr.2	6.38
	Zr.3	6.76
	Zr.4	7.60
	Zr.5	7.65
	Zr.6	6.65
	Zr.7	7.37
	Zr.8	6.48
	Zr.9	7.23
	Zr.10	7.13
	Zr.11	8.45
	Zr.12	7.05

with arc geochemical characteristics suggest that they may have formed in an island arc setting.

The Early Devonian Kangbutiebao Formation, which was invaded by the granite porphyries in the Kelang basin (Figure 2), is dominated by metasilicic pyroclasitic lavas with minor mafic volcanic rocks, including metarthyolite, metabasalt, metatuff, metavolcanic breccias and metavolcanic assemblages, which are consistent with those at active continental margins (Chai et al., 2009). The geochemical features of volcanic rocks from the Kangbutiebao Formation show bimodal geochemical characteristics, indicating a back-arc extensional regime (Xu et al., 2003; Chai et al., 2009; Wan et al., 2011). The coeval high-temperature metamorphic rocks, mafic rocks, adakitic and boninitic units (Xu et al., 2003; Niu et al., 2006; Jiang et al., 2010; Cai et al., 2012a; Cai et al., 2012b) demonstrate that the Early Devonian records the significant transfer of heat and juvenile material from the mantle to the crust. The subhorizontal, possibly extension-related, foliation (ca. 400 to 380 Ma) associated with high-temperature metamorphism occurs (Zhang J et al., 2015; Jiang et al., 2019). The above evidences support that the Chinese Altai was subjected to extensional tectonism during the Early Devonian. This condition could be met in the case of overriding plate crustal extension during trench retreat (Kemp et al., 2009; Collins et al., 2011; Zhang X R et al., 2015; Han et al., 2016; Nelson and Cottle, 2018; Li et al., 2019).

To discuss the Early Devonian tectonic setting, the geochemical data of coeval granitoids from the Chinese Altai are compiled. These granitoids belong to subalkaline granites (Figure 6A), medium-K to high-K calc-alkaline series (Figure 6B)

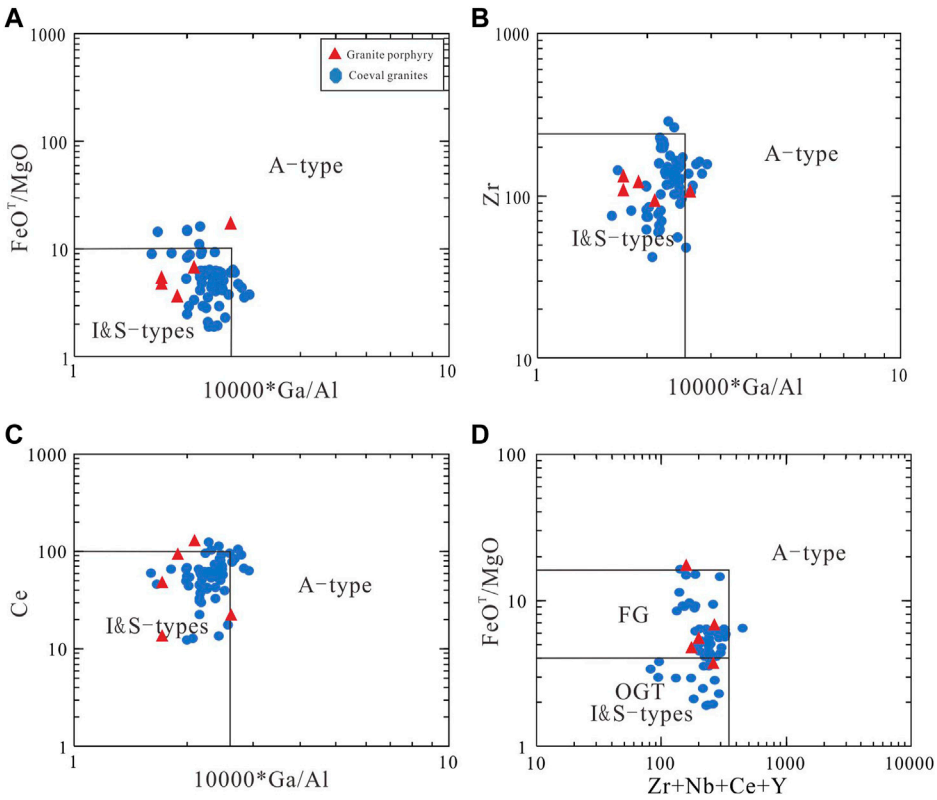

FIGURE 9
Discrimination diagrams of A-type granites from I- and S-type granites (Whalen et al., 1987). FG=fractionated granites; OGT=unfractionated I- and S-type granites. Other Early Devonian granitoid data are from Jiang (2021), Zheng et al. (2015), Tian (2018) and Yu et al. (2017).

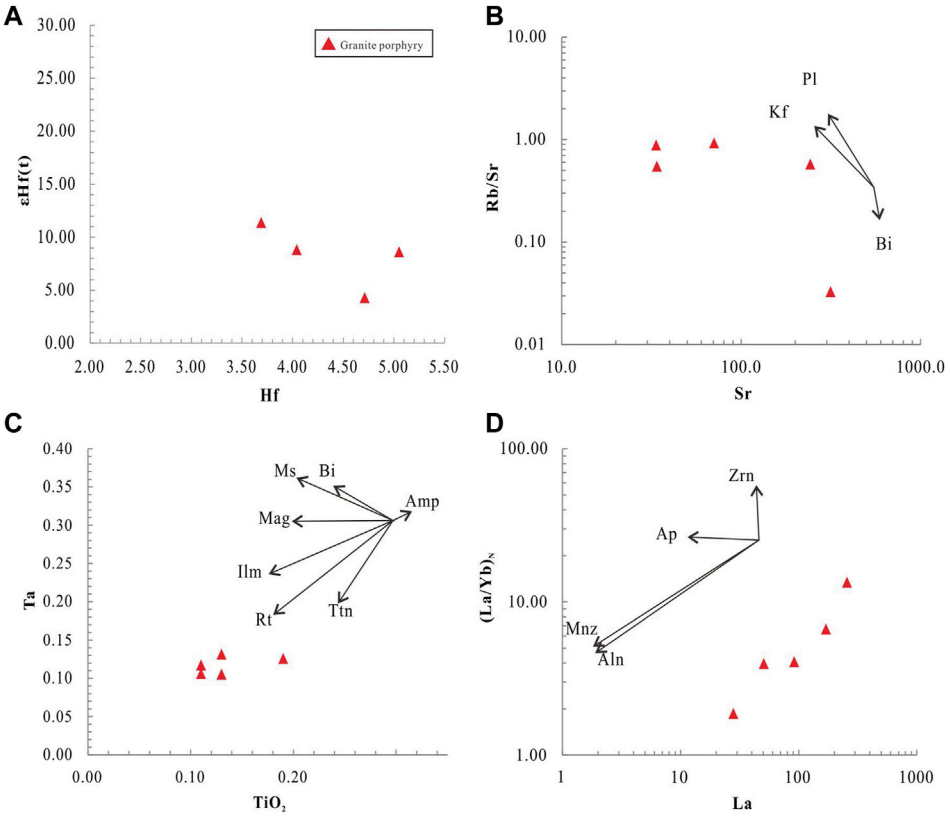

FIGURE 10
Diagrams of **(A)** $\varepsilon_{Hf}(t)$ *versus* Hf (ppm) contents; **(B)** Rb/Sr ratios *versus* Sr (ppm) contents; **(C)** Ta (ppm) contents *versus* TiO_2 (wt%) contents; **(D)** $(La/Yb)_N$ ratios *versus* La (ppm) contents. Pl=plagioclase; Kf=K-feldspar; Bi=biotite; Ms=muscovite; Amp=amphibole; Mag=magmatite; Ilm=ilmenite; Rt=tutile; Ttn=titanite; Zrn=zircon; Ap=apatite; Mnz=monazite; Aln=allanite.

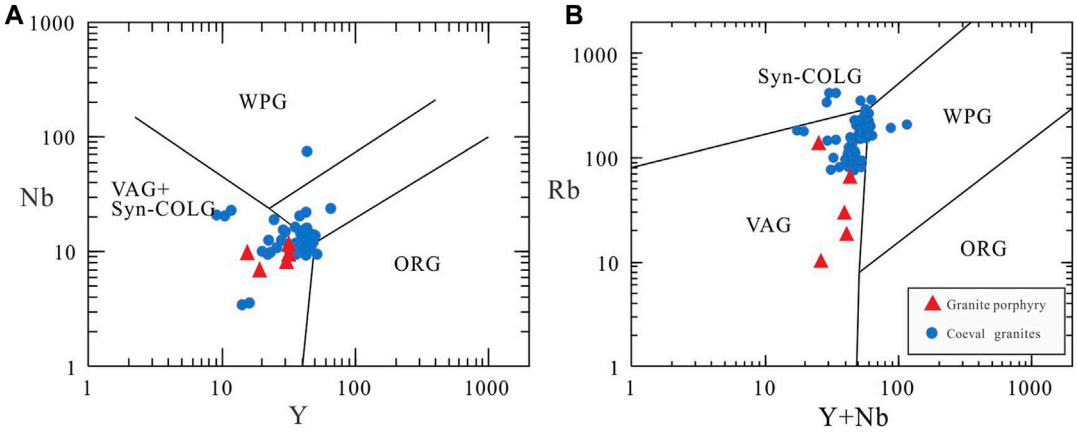

FIGURE 11
Tectonic discrimination diagrams of **(A)** Y (ppm) *versus* Nb (ppm) and **(B)** Y+Nb (ppm) *versus* Rb (ppm) (Pearce et al., 1984). Fields for Syn-COLG (syncollisional granite), VAG (volcanic arc granite), WPG (within-plate granite), and ORG (ocean-ridge granite) granites are from Pearce et al. (1984). Other Early Devonian granitoid data are from Jiang (2021), Zheng et al. (2015), Tian (2018) and Yu et al. (2017).

and metaluminous to peraluminous in composition (Figure 6C), with negative Eu, Nb, Ta and Ti anomalies and light REEs, Rb, Th and U enrichment (Figure 7). In addition, their compositions indicate that they are not A-type granites (Figure 9) but mostly I-type granites with A/CNK<1.1 (Figure 6C). The geochemical elements show similar curve characteristics to granite porphyries

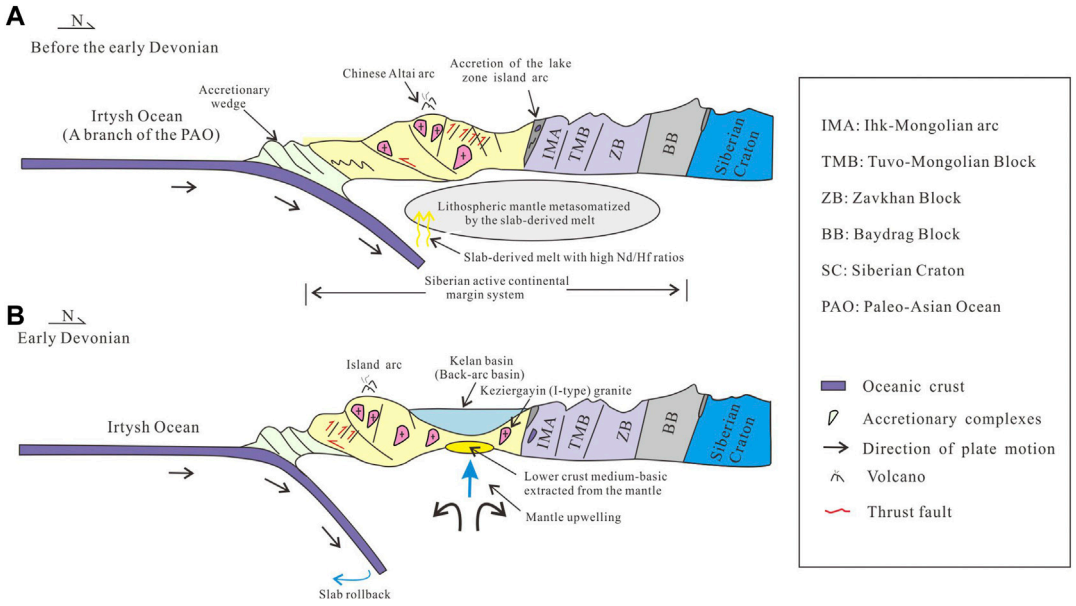

FIGURE 12
A tectonic model for the Chinese Altai during the early Devonian (or before).

(Figure 7). Within the element tectonic discrimination diagrams, most of these granitoids plot in the VAG field (Figure 11), further suggesting that the Early Devonian tectonic setting of the Chinese Altai was related to oceanic subduction.

In summary, we believe that there were island arcs and back-arc basins in the Chinese Altai during the Early Devonian, which belonged to the Siberian active continental margin system.

6.4.2 Implications for the geodynamic evolution of the Chinese Altai

The Chinese Altai experienced subduction, collision and accretion of different types of terrains and built up the current structural framework along with the closure of the Paleo-Asian Ocean (PAO) (Windley et al., 2002; Dobretsov et al., 2003; Xiao et al., 2004; Ni et al., 2006; Wang et al., 2006). Previous studies have shown that the Irtysh Ocean (a branch of the PAO) between the Junggar Block and Chinese Altai began to subduct northward at ~500 Ma, generating a series of blocks from south to north, namely, accretion of the lake zone island arc, Ikh-Mongol arc, Tuvo-Mongolian Block, Zavkhan Block and Baydrag Block in the Siberian continental margin (Li et al., 2019). Therefore, in the early Paleozoic, there was long-term subduction in the Chinese Altai, during which the lithospheric mantle was metasomatized by subducted slab-derived melts and resulted in Nd–Hf isotopic decoupling (Figure 12A).

As the main orogenic and mineralization period of the Chinese Altai, the Early Devonian is an important geological period to study the accretive orogenic process, continental crust growth mode and metallogenic geological background of bulk minerals. During this period, there are regional mutations in zircon isotope values. Two genetic models of mid-ocean ridge subduction (Cai et al., 2010; Jiang et al., 2010) and subducting slab rollback (Wang S J et al., 2020) have been proposed to explain this phenomenon.

This study reveals that there was a complete arc-basin system in the Chinese Altai. The local extension under the ocean subduction background produced bimodal volcanic rocks, high-temperature metamorphic rocks, mafic rocks, adakitic and boninitic units, indicating the existence of back-arc extension, which supports the subducting slab rollback model. The Chinese Altai experienced subducting slab rollback during the Early Devonian. In this process, early lower crust medium–basic igneous rocks, which were extracted from the lithospheric mantle underneath, are partially melted by the upwelling of the mantle, forming I-type granites after magma evolution, accompanied by pyroclastic deposition and regional deformation metamorphism (Figure 12B).

During the Early Devonian (or before), the ε_{Nd} (t) and ε_{Hf} (t) values of granitoids in the Chinese Altai are mostly positive (Wang et al., 2009; Cai et al., 2011c; Yu et al., 2017), and substantial granitoid rocks mainly made of juvenile materials intruded into the Altai orogenic belt, suggesting significant continental crust growth. These granitoids are all related to the subduction of the PAO, suggesting that continental formation was mainly achieved by lateral growth through subduction of multiple small blocks, island arcs, *etc.*, in the CAOB.

7 Conclusion

1) Zircon U–Pb dating reveals the presence of Early Devonian granite porphyry intrusions in the Kelan Basin, with a mean age of 394 ± 3 Ma.
2) The granite porphyries show geochemical affinity with I-type granite and originate from lower crust medium–basic igneous

rocks extracted from the lithospheric mantle metasomatized by subducted melt.

3) The Early Devonian arc-basin system associated with subducting slab rollback exists in the Chinese Altai, which can be attributed to the Siberian active continental margin system. These results reveal that the model of lateral accretion played a leading role in continental crustal growth during the Early Devonian (or before) in the CAOB.

Data availability statement

The original contributions presented in the study are included in the article/supplementary material, further inquiries can be directed to the corresponding author.

Author contributions

KW: Writing—original draft (lead) and investigation (lead); WK: Writing—original draft (supporting); XZ: Writing—review and editing (supporting); ZM: Investigation (supporting); JC: Investigation (supporting); QS: Writing—review and editing (supporting). All authors contributed to the article and approved the submitted version.

Funding

Financial support for this study was jointly provided by the Natural Science Basic Research Plan in Shaanxi Province (Nos. 2021JQ-329 and 2020JQ-440), Key R&D Program of Shaanxi Province (Nos. 2021KWZ-19 and 2022KW-19) and Geological Survey Project of China Geological Survey (Nos. DD20160105 and DD20190445).

Conflict of interest

The authors declare that the research was conducted in the absence of any commercial or financial relationships that could be construed as a potential conflict of interest.

Publisher's note

All claims expressed in this article are solely those of the authors and do not necessarily represent those of their affiliated organizations, or those of the publisher, the editors and the reviewers. Any product that may be evaluated in this article, or claim that may be made by its manufacturer, is not guaranteed or endorsed by the publisher.

References

Ahmed, H. A., Ma, C. Q., Wang, L. X., Palinkaš, L. A., Girei, M. B., Zhu, Y. X., et al. (2018). Petrogenesis and tectonic implications of peralkaline A-type granites and syenites from the Suizhou-Zaoyang Region, Central China. *J. Earth Sci.* 29, 1181–1202. doi:10.1007/s12583-018-0877-2

Ávila, J. N., Ireland, T. R., Holden, P., Lanc, P., Latimore, A., Schram, N., et al. (2020). High–precision, high–accuracy oxygen isotope measurements of zircon reference materials with the SHRIMP–SI. *Geostand. Geoanalytical Res.* 44, 85–102. doi:10.1111/ggr.12298

Badarch, G., Cunningham, W. D., and Windley, B. F. (2002). A new terrane subdivision for Mongolia: Implications for the phanerozoic crustal growth of central asia. *J. Asian Earth Sci.* 21, 87–110. doi:10.1016/s1367-9120(02)00017-2

Bao, G. J., Chai, F. M., Li, Y., Qi, D. M., Zhang, X. B., and Tian, M. (2021). Geochronology and geochemical characteristics of granitoids in the Bastielieke tungsten polymetallic deposit in the southern margin of Altay: Implications for tungsten mineralization. *Acta Petrol. Sin.* 37, 886–910. (in Chinese with English abstract). doi:10.18654/1000-0569/2021.03.15

Bonin, B. (2007). A-Type granites and related rocks: Evolution of a concept, problems and prospects. *Lithos* 97, 1–29. doi:10.1016/j.lithos.2006.12.007

Cai, K. D., Sun, M., Yuan, C., Long, X. P., and Xiao, W. J. (2011a). Geological framework and paleozoic tectonic history of the Chinese Altai, NW China: A review. *Russ. Geol. Geophys.* 52, 1619–1633. doi:10.1016/j.rgg.2011.11.014

Cai, K. D., Sun, M., Yuan, C., Xiao, W. J., Zhao, G. C., Long, X. P., et al. (2012a). Carboniferous mantle-derived felsic intrusion in the Chinese Altai, NW China: Implications for geodynamic change of the accretionary orogenic belt. *Gondwana Res.* 22, 681–698. doi:10.1016/j.gr.2011.11.008

Cai, K. D., Sun, M., Yuan, C., Zhao, G. C., Xiao, W. J., and Long, X. P. (2012b). Keketuohai mafic–ultramafic complex in the Chinese Altai, NW China: Petrogenesis and geodynamic significance. *Chem. Geol.* 294, 26–41. doi:10.1016/j.chemgeo.2011.11.031

Cai, K. D., Sun, M., Yuan, C., Zhao, G. C., Xiao, W. J., Long, X. P., et al. (2010). Geochronological and geochemical study of mafic dykes from the northwest Chinese Altai: Implications for petrogenesis and tectonic evolution. *Gondwana Res.* 18, 638–652. doi:10.1016/j.gr.2010.02.010

Cai, K. D., Sun, M., Yuan, C., Zhao, G. C., Xiao, W. J., Long, X. P., et al. (2011b). Geochronology, petrogenesis and tectonic significance of peraluminous granites from the Chinese Altai, NW China. *Lithos* 127, 261–281. doi:10.1016/j.lithos.2011.09.001

Cai, K. D., Sun, M., Yuan, C., Zhao, G. C., Xiao, W. J., Long, X. P., et al. (2011c). Prolonged magmatism, juvenile nature and tectonic evolution of the Chinese Altai, NW China: Evidence from zircon U–Pb and Hf isotopic study of paleozoic granitoids. *J. Asian Earth Sci.* 42, 949–968. doi:10.1016/j.jseaes.2010.11.020

Chai, F. M., Mao, J. W., Dong, L. H., Yang, F. Q., Liu, F., Geng, X. X., et al. (2009). Geochronology of metarhyolites from the Kangbutiebao Formation in the Kelang basin, Altay mountains, Xinjiang: Implications for the tectonic evolution and metallogeny. *Gondwana Res.* 16, 189–200. doi:10.1016/j.gr.2009.03.002

Chappell, B. W., Bryant, C. J., and Wyborn, D. (2012). Peraluminous I-type granites. *Lithos* 153, 142–153. doi:10.1016/j.lithos.2012.07.008

Chappell, B. W. (1974). Two contrasting granite types. *Pac. Geol.* 8, 173–174.

Chappell, B. W., and White, A. J. R. (1992). I-And S-type granites in the lachlan fold belt. *Earth Environ. Sci. Trans. R. Soc. Edinb.* 83, 1–26. doi:10.1017/s0263593300007720

Chen, B., and Jahn, B. (2002). Geochemical and isotopic studies of the sedimentary and granitic rocks of the Altai orogen of northwest China and their tectonic implications. *Geol. Mag.* 139, 1–13. doi:10.1017/s0016756801006100

Chen, Y. W., Hu, R. Z., Bi, X. W., Dong, S. H., Xu, Y., and Zhou, T. (2018). Zircon U–Pb ages and Sr-Nd-Hf isotopic characteristics of the Huichizi granitic complex in the North Qinling Orogenic Belt and their geological significance. *J. Earth Sci.* 29, 492–507. doi:10.1007/s12583-017-0906-6

Coleman, R. G. (1989). Continental growth of northwest China. *Tectonics* 8, 621–635. doi:10.1029/tc008i003p00621

Collins, W. J., Beams, S. D., White, A. J. R., and Chappell, B. W. (1982). Nature and origin of A-type granites with particular reference to southeastern Australia. *Contributions Mineralogy Petrology* 80, 189–200. doi:10.1007/bf00374895

Collins, W. J., Belousova, E. A., Kemp, A. I., and Murphy, J. B. (2011). Two contrasting Phanerozoic orogenic systems revealed by hafnium isotope data. *Nat. Geosci.* 4, 333–337. doi:10.1038/ngeo1127

Dobretsov, N. L., Buslov, M. M., and Vernikovsky, V. A. (2003). Neoproterozoic to early ordovician evolution of the Paleo-Asian ocean: Implications to the break-up of rodinia. *Gondwana Res.* 6, 143–159. doi:10.1016/s1342-937x(05)70966-7

Farina, F., Stevens, G., Gerdes, A., and Frei, D. (2014). Small-scale Hf isotopic variability in the peninsula pluton (south Africa): The processes that control inheritance of source $^{176}Hf/^{177}Hf$ diversity in S-type granites. *Contributions Mineralogy Petrology* 168, 1065–1118. doi:10.1007/s00410-014-1065-8

Gao, P., Zheng, Y. F., and Zhao, Z. F. (2016). Experimental melts from crustal rocks: A lithochemical constraint on granite petrogenesis. *Lithos* 266, 133–157. doi:10.1016/j.lithos.2016.10.005

Gao, S., Rudnick, R. L., Xu, W. L., Yuan, H. L., Liu, Y. S., Walker, R. J., et al. (2008). Recycling deep cratonic lithosphere and generation of intraplate magmatism in the North China Craton. *Earth Planet. Sci. Lett.* 270, 41–53. doi:10.1016/j.epsl.2008.03.008

Geng, H. Y., Sun, M., Yuan, C., Xiao, W. J., Xian, W. S., Zhao, G. C., et al. (2009). Geochemical, Sr–Nd and zircon U–Pb–Hf isotopic studies of late carboniferous magmatism in the west junggar, Xinjiang: Implications for ridge subduction? *Chem. Geol.* 266, 364–389. doi:10.1016/j.chemgeo.2009.07.001

Griffin, W. L., Wang, X., Jackson, S. E., Pearson, N. J., O'Reilly, S. Y., Xu, X. S., et al. (2002). Zircon chemistry and magma mixing, SE China: *In situ* analysis of Hf isotopes, tonglu and pingtan igneous complexes. *Lithos* 61, 237–269. doi:10.1016/s0024-4937(02)00082-8

Han, B. F., Wang, S. G., Jahn, B., Hong, D. W., Kagami, H., and Sun, Y. L. (1997). Depleted-mantle source for the ulungur river A-type granites from north Xinjiang, China: Geochemistry and Nd–Sr isotopic evidence, and implications for phanerozoic crustal growth. *Chem. Geol.* 138, 135–159. doi:10.1016/s0009-2541(97)00003-x

Han, Y. G., Zhao, G. C., Cawood, P. A., Sun, M., Eizenhöfer, P. R., Hou, W. Z., et al. (2016). Tarim and North China cratons linked to northern Gondwana through switching accretionary tectonics and collisional orogenesis. *Geology* 44, 95–98. doi:10.1130/g37399.1

Holden, P., Halliday, A. N., and Stephens, W. E. (1987). Neodymium and strontium isotope content of microdiorite enclaves points to mantle input to granitoid production. *Nature* 330, 53–56. doi:10.1038/330053a0

Irvine, T. N., and Baragar, W. R. A. (1971). A guide to the chemical classification of the common volcanic rocks. *Can. J. Earth Sci.* 8, 523–548. doi:10.1139/e71-055

Jahn, B. (2004). The central asian orogenic belt and growth of the continental crust in the phanerozoic. *Geol. Soc. Lond. Spec. Publ.* 226, 73–100. doi:10.1144/gsl.sp.2004.226.01.05

Jahn, B., Wu, F. C., Capdevila, R., Martineau, F., Zhao, Z. H., and Wang, Y. X. (2001). Highly evolved juvenile granites with tetrad REE patterns: The woduhe and baerzhe granites from the great xing'an mountains in NE China. *Lithos* 59, 171–198. doi:10.1016/s0024-4937(01)00066-4

Jahn, B., Wu, F. Y., and Chen, B. (2000a). Granitoids of the central asian orogenic belt and continental growth in the phanerozoic. *Earth Environ. Sci. Trans. R. Soc. Edinb.* 91, 181–193. doi:10.1017/s0263593300007367

Jahn, B., Wu, F. Y., and Chen, B. (2000b). Massive granitoid generation in central asia: Nd isotope evidence and implication for continental growth in the phanerozoic. *Episodes J. Int. Geoscience* 23, 82–92. doi:10.18814/epiiugs/2000/v23i2/001

Jiang, L. (2021). *Genesis of the granite in the northeast of Altay and its constraints on the paleozoic tectonic evolution process of the Altai orogenic belt*. Dissertation Submitted to Northwest University for Master's Degree. United States: Northwest University.

Jiang, Y. D., Schulmann, K., Sun, M., Weinberg, R. F., Štípská, P., Li, P. F., et al. (2019). Structural and geochronological constraints on Devonian suprasubduction tectonic switching and Permian collisional dynamics in the Chinese Altai, Central Asia. *Tectonics* 38, 253–280. doi:10.1029/2018tc005231

Jiang, Y. D., Sun, M., Zhao, G. C., Yuan, C., Xiao, W. J., Xia, X. P., et al. (2010). The~390 Ma high-T metamorphic event in the Chinese Altai: A consequence of ridge-subduction? *Am. J. Sci.* 310, 1421–1452. doi:10.2475/10.2010.08

Jiang, Y. H., Jiang, S. Y., Ling, H. F., and Dai, B. Z. (2006). Low-degree melting of a metasomatized lithospheric mantle for the origin of cenozoic yulong monzogranite-porphyry, east tibet: Geochemical and Sr–Nd–Pb–Hf isotopic constraints. *Earth Planet. Sci. Lett.* 241, 617–633. doi:10.1016/j.epsl.2005.11.023

Kemp, A. I. S., Hawkesworth, C. J., Collins, W. J., Gray, C. M., and Blevin, P. L. (2009). Isotopic evidence for rapid continental growth in an extensional accretionary orogen: The Tasmanides, eastern Australia. *Earth Planet. Sci. Lett.* 284, 455–466. doi:10.1016/j.epsl.2009.05.011

Khain, E. V., Bibikova, E. V., Kröner, A., Zhuravlev, D. Z., Sklyarov, E. V., Fedotova, A. A., et al. (2002). The most ancient ophiolite of the central asian fold belt: U–Pb and Pb–Pb zircon ages for the dunzhugur complex, eastern sayan, Siberia, and geodynamic implications. *Earth Planet. Sci. Lett.* 199, 311–325. doi:10.1016/s0012-821x(02)00587-3

King, P. L., White, A. J. R., Chappell, B. W., and Allen, C. M. (1997). Characterization and origin of aluminous A-type granites from the Lachlan Fold Belt, southeastern Australia. *J. Petrology* 38, 371–391. doi:10.1093/petroj/38.3.371

Kröner, A., Kovach, V., Belousova, E., Hegner, E., Armstrong, R., Dolgopolova, A., et al. (2014). Reassessment of continental growth during the accretionary history of the central asian orogenic belt. *Gondwana Res.* 25, 103–125. doi:10.1016/j.gr.2012.12.023

Li, P. F., Sun, M., Shu, C. T., Yuan, C., Jiang, Y. D., Zhang, L., et al. (2019). Evolution of the central asian orogenic belt along the siberian margin from neoproterozoic-early paleozoic accretion to devonian trench retreat and a comparison with phanerozoic eastern Australia. *Earth-Science Rev.* 198, 102951. doi:10.1016/j.earscirev.2019.102951

Li, X. H., Li, Z. X., Li, W. X., Liu, Y., Yuan, C., Wei, G., et al. (2007). U–Pb zircon, geochemical and Sr–Nd–Hf isotopic constraints on age and origin of jurassic I-and A-type granites from central guangdong, SE China: A major igneous event in response to foundering of a subducted flat-slab? *Lithos* 96, 186–204. doi:10.1016/j.lithos.2006.09.018

Liu, F., Li, Y. H., Mao, J. W., Yang, F. Q., Chai, F. M., Geng, X. X., et al. (2008). The SHRIMP U–Pb ages of Abagong granites in the Altaid Orogen and its geologic implication. *Acta Geosci. Sin.* 29, 795–804. (in Chinese with English abstract).

Liu, W., Liu, C. Q., and Masuda, A. (1997). Complex trace-element effects of mixing-fractional crystallization composite processes: Applications to the alaer granite pluton, Altay mountains, Xinjiang, northwestern China. *Chem. Geol.* 135, 103–124. doi:10.1016/s0009-2541(96)00111-8

Long, X. P., Sun, M., Yuan, C., Xiao, W. J., Lin, S. F., Wu, F. Y., et al. (2007). Detrital zircon age and Hf isotopic studies for metasedimentary rocks from the Chinese Altai: Implications for the early paleozoic tectonic evolution of the central asian orogenic belt. *Tectonics* 26. doi:10.1029/2007tc002128

Long, X. P., Yuan, C., Sun, M., Xiao, W. J., Zhao, G. C., Wang, Y., et al. (2010). Detrital zircon ages and Hf isotopes of the early paleozoic flysch sequence in the Chinese Altai, NW China: New constrains on depositional age, provenance and tectonic evolution. *Tectonophysics* 480, 213–231. doi:10.1016/j.tecto.2009.10.013

Ludwig, K. R. (2003). Isoplot 3.00: A geochronological toolkit for microsoft excel. *Berkeley Geochronol. Cent. Spec. Publ.* 4, 1–70.

Ma, Q., Zheng, J. P., Griffin, W. L., Zhang, M., Tang, H. Y., Su, Y. P., et al. (2012). Triassic "adakitic" rocks in an extensional setting (north China): Melts from the cratonic lower crust. *Lithos* 149, 159–173. doi:10.1016/j.lithos.2012.04.017

Maniar, P. D., and Piccoli, P. M. (1989). Tectonic discrimination of granitoids. *Geol. Soc. Am. Bull.* 101, 635–643. doi:10.1130/0016-7606(1989)101<0635:tdog>2.3.co;2

Middlemost, E. A. (1994). Naming materials in the magma/igneous rock system. *Earth-Science Rev.* 37, 215–224. doi:10.1016/0012-8252(94)90029-9

Mossakovsky, A. (1993). Central asian fold belt: Geodynamic evolution and history of formation. *Geotectonics* 6, 3–33.

Nelson, D. A., and Cottle, J. M. (2018). The secular development of accretionary orogens: Linking the gondwana magmatic arc record of west Antarctica, Australia and south America. *Gondwana Res.* 63, 15–33. doi:10.1016/j.gr.2018.06.002

Ni, Z. Y., Zhai, M. G., Wang, R. M., and Tong, Y. (2006). Late paleozoic retrograded eclogites from within the northern margin of the North China craton: Evidence for subduction of the Paleo-Asian Ocean. *Gondwana Res.* 9, 209–224. doi:10.1016/j.gr.2005.06.014

Niu, H. C., Sato, H., Zhang, H. X., Ito, J., Yu, X. Y., Nagao, T., et al. (2006). Juxtaposition of adakite, boninite, high-TiO_2 and low-TiO_2 basalts in the Devonian southern Altay, Xinjiang, NW China. *J. Asian Earth Sci.* 28, 439–456. doi:10.1016/j.jseaes.2005.11.010

Pearce, J. A., Harris, N. B., and Tindle, A. G. (1984). Trace element discrimination diagrams for the tectonic interpretation of granitic rocks. *J. Petrology* 25, 956–983. doi:10.1093/petrology/25.4.956

Pearce, J. A., Kempton, P. D., Nowell, G. M., and Noble, S. R. (1999). Hf-Nd element and isotope perspective on the nature and provenance of mantle and subduction components in Western Pacific arc-basin systems. *J. Petrology* 40, 1579–1611. doi:10.1093/petroj/40.11.1579

Peccerillo, A., and Taylor, S. R. (1976). Geochemistry of Eocene calc-alkaline volcanic rocks from the Kastamonu area, northern Turkey. *Contributions Mineralogy Petrology* 58, 63–81. doi:10.1007/bf00384745

Şengör, A. M. C., Natal'In, B. A., and Burtman, V. S. (1993). Evolution of the Altaid tectonic collage and Palaeozoic crustal growth in Eurasia. *Nature* 364, 299–307. doi:10.1038/364299a0

Shen, X. M., Zhang, H. X., Wang, Q., Saha, A., and Ma, L. (2017). Zircon U–Pb geochronology and geochemistry of devonian plagiogranites in the Kuerti area of southern Chinese Altay, northwest China: Petrogenesis and tectonic evolution of late paleozoic ophiolites. *Geol. J.* 53, 1886–1905. doi:10.1002/gj.3020

Song, B. (2002). Mount making and procedure of the SHRIMP dating. *Geol. Rev.* 48, 26–30.

Spandler, C., Mavrogenes, J., and Hermann, J. (2007). Experimental constraints on element mobility from subducted sediments using high-P synthetic fluid/melt inclusions. *Chem. Geol.* 239, 228–249. doi:10.1016/j.chemgeo.2006.10.005

Sun, M., Long, X. P., Cai, K. D., Jiang, Y. D., Wang, B. Y., Yuan, C., et al. (2009). Early paleozoic ridge subduction in the Chinese Altai: Insight from the abrupt change in zircon Hf isotopic compositions. *Sci. China Ser. D Earth Sci.* 52, 1345–1358. doi:10.1007/s11430-009-0110-3

Sun, M., Yuan, C., Xiao, W. J., Long, X. P., Xia, X. P., Zhao, G. C., et al. (2008). Zircon U–Pb and Hf isotopic study of gneissic rocks from the Chinese Altai: Progressive accretionary history in the early to middle Palaeozoic. *Chem. Geol.* 247, 352–383. doi:10.1016/j.chemgeo.2007.10.026

Sun, S. S., and McDonough, W. F. (1989). Chemical and isotopic systematics of oceanic basalts: Implications for mantle composition and processes. *Geol. Soc. Lond. Spec. Publ.* 42, 313–345. doi:10.1144/gsl.sp.1989.042.01.19

Taylor, S. R., and McLennan, S. M. (1985). *The continental crust: Its composition and evolution*. Carlton: Blackwell Scientific Publication, 1–312.

Tian, H. (2018). *The Paleozoic to Mesozoic magmatism and tectonic evolution of the central Altay tectonic belt, Xinjiang, China*. Master`s Degree. Beijing: Dissertation Submitted to China University of Geosciences.

Todd, E., Gill, J. B., Wysoczanski, R. J., Handler, M. R., Wright, I. C., and Gamble, J. A. (2010). Sources of constructional cross-chain volcanism in the southern Havre Trough: New insights from HFSE and REE concentration and isotope systematics. *Geochem. Geophys. Geosystems* 11, 1–31. doi:10.1029/2009gc002888

Wan, B., Xiao, W. J., Zhang, L. C., Windley, B. F., Han, C. M., and Quinn, C. D. (2011). Contrasting styles of mineralization in the Chinese Altai and east junggar, NW China: Implications for the accretionary history of the southern altaids. *J. Geol. Soc.* 168, 1311–1321. doi:10.1144/0016-76492011-021

Wang J, J., Su, Y. P., Zheng, J. P., Belousova, E. A., Chen, M., Dai, H. K., et al. (2020). Slab roll-back triggered back-arc extension south of the Paleo-Asian Ocean: Insights from Devonian MORB-like diabase dykes from the Chinese Altai. *Lithos* 376, 105790. doi:10.1016/j.lithos.2020.105790

Wang S J, S. J., Schertl, H. P., and Pang, Y. M. (2020). Geochemistry, geochronology and Sr–Nd–Hf isotopes of two types of early Cretaceous granite porphyry dykes in the Sulu orogenic belt, eastern China. *Can. J. Earth Sci.* 57, 249–266. doi:10.1139/cjes-2019-0003

Wang, T., Hong, D. W., Jahn, B., Tong, Y., Wang, Y. B., Han, B. F., et al. (2006). Timing, petrogenesis, and setting of paleozoic synorogenic intrusions from the Altai mountains, northwest China: Implications for the tectonic evolution of an accretionary orogen. *J. Geol.* 114, 735–751. doi:10.1086/507617

Wang, T., Huang, H., Zhang, J. J., Wang, C. Y., Cao, G. Y., Xiao, W. J., et al. (2023). Voluminous continental growth of the Altaids and its control on metallogeny. *Natl. Sci. Rev.* 10, nwac283. doi:10.1093/nsr/nwac283

Wang, T., Jahn, B. M., Kovach, V. P., Tong, Y., Hong, D. W., and Han, B. F. (2009). Nd–Sr isotopic mapping of the Chinese Altai and implications for continental growth in the Central Asian Orogenic Belt. *Lithos* 110, 359–372. doi:10.1016/j.lithos.2009.02.001

Weng, K., Dong, Y. P., Jiang, L. Q., Ma, Z. P., Wang, S. S., and Chen, B. (2023). Geochemistry, geochronology and Sr-Nd-Hf isotopes of Paleozoic granitoids in the Chinese Altai, NW China: Constraints on the conversion from subduction-accretion to syn/post-collision. *J. Geol. Soc.* 108, 1–22. doi:10.1144/jgs2022-150

Whalen, J. B., Currie, K. L., and Chappell, B. W. (1987). A-Type granites: Geochemical characteristics, discrimination and petrogenesis. *Contributions Mineralogy Petrology* 95, 407–419. doi:10.1007/bf00402202

White, A. J. R., and Chappell, B. W. (1983). Granitoid types and their distribution in the Lachlan Fold Belt, southeastern Australia. *Geol. Soc. Am. Mem.* 159, 21–34.

Wilhem, C., Windley, B. F., and Stampfli, G. M. (2012). The altaids of central asia: A tectonic and evolutionary innovative review. *Earth-Science Rev.* 113, 303–341. doi:10.1016/j.earscirev.2012.04.001

Windley, B. F., Alexeiev, D., Xiao, W. J., Kröner, A., and Badarch, G. (2007). Tectonic models for accretion of the central asian orogenic belt. *J. Geol. Soc.* 164, 31–47. doi:10.1144/0016-76492006-022

Windley, B. F., Kröner, A., Guo, J. H., Qu, G. S., Li, Y. Y., and Zhang, C. (2002). Neoproterozoic to paleozoic geology of the Altai orogen, NW China: New zircon age data and tectonic evolution. *J. Geol.* 110, 719–737. doi:10.1086/342866

Xiao, Q. H., Wang, T., Deng, J. F., Mo, X. X., Lu, X. X., Hong, D. W., et al. (2009). *Granitoids and continent growth of key Orogene in China*. Beijing: Geological Publishing House, 1–528. (in Chinese).

Xiao, W. J., Windley, B. F., Badarch, G., Sun, S., Li, J., Qin, K., et al. (2004). Palaeozoic accretionary and convergent tectonics of the southern altaids: Implications for the growth of central asia. *J. Geol. Soc.* 161, 339–342. doi:10.1144/0016-764903-165

Xu, J. F., Castillo, P. R., Chen, F. R., Niu, H. C., Yu, X. Y., and Zhen, Z. P. (2003). Geochemistry of late paleozoic mafic igneous rocks from the Kuerti area, Xinjiang, northwest China: Implications for backarc mantle evolution. *Chem. Geol.* 193, 137–154. doi:10.1016/s0009-2541(02)00265-6

Yang, F. Q., Chai, F. M., Li, Q., Gu, G. L., and Yang, C. D. (2017). The discovery of the late cambrian-early ordovician strata in the basement of the Kelan basin, Altay, Xinjiang: Constrains from zircon LA-MC-ICP–MS U–Pb dating. *Acta Geosci. Sin.* 38, 859–871.

Yang, F. Q., Li, Y., Chen, G. M., Zhang, G. F., Li, C., Tian, M., et al. (2019). Ore-forming age of the Basitielieke tungsten polymetallic deposit in the Altay, Xinjiang: Constraits of zircon U–Pb and molybdenite Re–Os geochronology. *Geotect. Metallogenia* 43, 1144–1154.

Yang, F. Q., Mao, J. W., Yan, S. H., Liu, F., Chai, F. M., Zhou, G., et al. (2008). Geochronology, geochemistry and geological implications of the Mengku synorogenic plagiogranite pluton in Altay, Xinjiang. *Acta Geol. Sin.* 82, 485–499.

Yang, F. Q., Zhang, B., Yang, C. D., Li, Q., and Wang, Y. Q. (2021). Geology and geochronology of the volcanogenic massive sulphide polymetallic deposits in Altay orogenic belt, Xinjiang, northwest China: Examples from the Kelan Basin. *Int. Geol. Rev.* 63, 1199–1214. doi:10.1080/00206814.2020.1756001

Yang, G. X., Li, Y. J., Tong, L. L., Wang, Z. P., Si, G. H., Lindagato, P., et al. (2022). Natural observations of subduction initiation: Implications for the geodynamic evolution of the Paleo-Asian Ocean. *Paleo-Asian Ocean. Geosystems Geoenvironment* 1, 100009. doi:10.1016/j.geogeo.2021.10.004

Yang, G. X., Li, Y. J., Xiao, W. J., and Tong, L. L. (2015). OIB-Type rocks within west junggar ophiolitic mélanges: Evidence for the accretion of seamounts. *Earth-Science Rev.* 150, 477–496. doi:10.1016/j.earscirev.2015.09.002

Yu, Y., Sun, M., Long, X. P., Li, P. F., Zhao, G. C., Kröner, A., et al. (2017). Whole-rock Nd–Hf isotopic study of I-type and peraluminous granitic rocks from the Chinese Altai: Constraints on the nature of the lower crust and tectonic setting. *Gondwana Res.* 47, 131–141. doi:10.1016/j.gr.2016.07.003

Yuan, C., Sun, M., Xiao, W. J., Li, X. H., Chen, H. L., Lin, S. F., et al. (2007). Accretionary orogenesis of the Chinese Altai: Insights from paleozoic granitoids. *Chem. Geol.* 242, 22–39. doi:10.1016/j.chemgeo.2007.02.013

Zhang, C., Liu, L. F., Santosh, M., Luo, Q., and Zhang, X. (2017). Sediment recycling and crustal growth in the central asian orogenic belt: Evidence from Sr–Nd–Hf isotopes and trace elements in granitoids of the Chinese Altay. *Gondwana Res.* 47, 142–160. doi:10.1016/j.gr.2016.08.009

Zhang, H. X., Niu, H. C., Terada, K., Yu, X. Y., Sato, H., and Ito, J. (2003). Zircon SHRIMP U-Pb dating on plagiogranite from Kuerti ophiolite in Altay, north Xinjiang. *Chin. Sci. Bull.* 48, 2231–2235. (in Chinese). doi:10.1007/bf03182858

Zhang, J., Sun, M., Schulmann, K., Zhao, G. C., Wu, Q. H., Jiang, Y. D., et al. (2015). Distinct deformational history of two contrasting tectonic domains in the Chinese Altai: Their significance in understanding accretionary orogenic process. *J. Struct. Geol.* 73, 64–82. doi:10.1016/j.jsg.2015.02.007

Zhang, X. R., Zhao, G. C., Sun, M., Eizenhöfer, P. R., Han, Y. G., Hou, W. Z., et al. (2015). Tectonic evolution from subduction to arc-continent collision of the Junggar ocean: Constraints from U–Pb dating and Hf isotopes of detrital zircons from the North Tianshan belt, NW China. *Bulletin* 128, 644–660. doi:10.1130/b31230.1

Zhao, X. C., Zhou, W. X., Fu, D., Huang, B., and Ge, M. C. (2018). Isotope chronology and geochemistry of the lower carboniferous granite in xilinhot, inner Mongolia, China. *J. Earth Sci.* 29, 280–294. doi:10.1007/s12583-017-0942-2

Zheng, J. H., Mao, J. W., Yang, F. Q., Liu, F., and Zhu, Y. F. (2015). The postcollisional Cihai iron skarn deposit, eastern Tianshan, Xinjiang, China. *Ore Geol. Rev.* 67, 244–254. doi:10.1016/j.oregeorev.2014.12.006

Zhong, H., Zhu, W. G., Chu, Z. Y., He, D. F., and Song, X. Y. (2007). SHRIMP U–Pb zircon geochronology, geochemistry, and Nd–Sr isotopic study of contrasting granites in the Emeishan large igneous province, SW China. *Chem. Geol.* 236, 112–133. doi:10.1016/j.chemgeo.2006.09.004

Zhou, G., Zhang, Z. C., Luo, S. B., He, B., Wang, X., Yin, L. J., et al. (2007). Confirmation of high-temperature strongly peraluminous mayin'ebo granites in the south margin of Altay, Xinjiang: Age, geochemistry and tectonic implications. *Acta Petrol. Sin.* 23, 1909–1920.

Zhu, Y., Chen, B. O., and Qiu, T. (2015). Geology and geochemistry of the baijiantan–baikouquan ophiolitic mélanges: Implications for geological evolution of west junggar, Xinjiang, NW China. *Geol. Mag.* 152, 41–69. doi:10.1017/s0016756814000168

Zhu, Y. F., Zeng, Y., and Gu, L. (2006). Geochemistry of the rare metal-bearing pegmatite No. 3 vein and related granites in the Keketuohai region, Altay Mountains, northwest China. *J. Asian Earth Sci.* 27, 61–77. doi:10.1016/j.jseaes.2005.01.007

Zhu, Y., and Ogasawara, Y. (2002). Carbon recycled into deep Earth: Evidence from dolomite dissociation in subduction-zone rocks. *Geology* 30, 947–950. doi:10.1130/0091-7613(2002)030<0947:cridee>2.0.co;2

Zonenshain, L. P. (1990). Geology of the USSR: A plate tectonic synthesis. *Geodyn. Monogr.* 21, 1–242.